Geomorphology 415 (2022) 108386

Contents lists available at ScienceDirect

Geomorphology

journal homepage: www.journals.elsevier.com/geomorphology

Mechanisms of rock slope failures triggered by the 2016 Mw 7.8 Kaikōura earthquake and implications for landslide susceptibility

Corinne Singeisen [a,*], Chris Massey [b], Andrea Wolter [b], Richard Kellett [b], Colin Bloom [a], Tim Stahl [a], Caleb Gasston [c], Katie Jones [b,d]

[a] University of Canterbury, Christchurch, New Zealand
[b] GNS Science, Lower Hutt, New Zealand
[c] University of Auckland, Auckland, New Zealand
[d] Victoria University of Wellington, Wellington, New Zealand

ARTICLE INFO

Keywords:
Slope stability
Failure mechanism
Landslide susceptibility
Coseismic landslide
Kaikōura earthquake

ABSTRACT

Landslide failure mechanisms are influenced by topography, lithology, structure and rock mass damage – factors that also control landslide susceptibility. Failure mechanisms, however, are rarely considered in regional-scale coseismic landslide susceptibility analyses. In this study, we use 3D pixel tracking in pre- and post-earthquake aerial imagery, geomorphic mapping, rock mass characterisation, and geophysical ground investigations to develop conceptual models for three earthquake-induced landslides triggered by the 2016 Mw 7.8 Kaikōura earthquake on New Zealand's South Island. Analysis of two incipient landslides in Cretaceous greywacke illustrates the failure stages of a rock mass comprising multiple sets of closely-spaced and low persistence discontinuities. Conversely, analysis of a landslide in Neogene massive siltstones illustrates the role of high-persistence bedding planes in generating large translational rockslides. These two distinct mechanisms typify failures in highly deformed basement and overlying massive sedimentary rocks respectively, and highlight the link between rock mass damage, failure mechanism, and initiation. In greywacke failures, the rupture plane initiated close to the ridgetop and propagated as a joint-step-path failure along pre-existing, but low-persistence joints whereas the landslide in Neogene siltstone initiated by sliding along weak, high persistence, bedding planes near the base of the slope where topographic stresses are highest. Analysis of landslide displacements furthermore points out that the evolution of landslides is closely related to rock mass characteristics. In highly jointed Cretaceous greywacke, relatively little displacement is needed for rock mass disintegration and avalanching to occur whereas in Neogene siltstone, the landslide displaces as a coherent body - even at large displacements.

Our results suggest that (1) failure mechanisms and, as a result, coseismic landslide susceptibility factors, may vary fundamentally in different geological settings; (2) characteristic spatial landslide displacement patterns may be used to remotely identify relevant failure mechanisms; and (3) the amount of displacement that can be accommodated before a failure transitions from sliding to avalanching, is highly dependent on material characteristics and topographic constraints.

1. Introduction

In tectonically active regions, faulting and folding build topography, reduce rock mass strength, control bedrock structure — and therefore predispose the landscape to landslides (Terzaghi, 1962; Gerber and Scheidegger, 1969; Korup, 2004; Gallen et al., 2014; McColl, 2015; Stead and Wolter, 2015; Upton et al., 2018). Additionally, weathering and stress-induced fatigue can lead to rock mass damage through fracturing and rock strength degradation and further prepare slopes to fail (Brideau et al., 2009; Gischig et al., 2016; Grämiger et al., 2017; Donati et al., 2021). While landslides in tectonically active regions frequently occur with no apparent trigger, many are triggered during large earthquakes or heavy rainfall (Keefer, 1984; Tanyaş et al., 2017; Fan et al., 2019).

During an earthquake, the static stress state of a rock slope is perturbed due to seismic ground motion (Murphy, 2006). Topographic and

* Corresponding author.
E-mail address: corinne.singeisen@pg.canterbury.ac.nz (C. Singeisen).

https://doi.org/10.1016/j.geomorph.2022.108386
Received 3 March 2022; Received in revised form 27 July 2022; Accepted 28 July 2022
Available online 8 August 2022

geological site effects may further enhance ground acceleration through amplification that is typically highest near the slope crest (Benites and Haines, 1994; Meunier et al., 2008; Gischig et al., 2015; Massey et al., 2017; Dafni and Wartman, 2021). These transient stresses may trigger slope failure or, if failure does not occur, prepare the slope for failure in a future event (Marc et al., 2015; Parker et al., 2015; Gischig et al., 2016).

Other triggers and preparatory factors such as rainfall events, permafrost degradation, weathering, and erosion influence slope stability through increased pore water pressure, strength reduction and increase of static topographic stresses (Terzaghi, 1962; Krautblatter et al., 2013; Viles, 2013; Krautblatter and Moore, 2014; Bilderback et al., 2015). In these cases, failure initiation typically occurs at the toe of the slope where topographic stresses are highest (Eberhardt et al., 2004).

The same topographic and rock mass characteristics that control landslide initiation also govern failure mechanism (Brideau et al., 2009; Agliardi et al., 2013; Stead and Wolter, 2015). For example, if few persistent discontinuities are present, slopes typically fail through structural control (Fig. 1 A). These structurally-controlled failures are well understood and are the basis of first-order rock slope stability assessment through kinematic analysis (Hoek and Bray, 1981). In contrast, in rock masses without persistent discontinuities, failure commonly occurs through a step-path mechanism that can include breaking of intact rock bridges (Eberhardt et al., 2004; Brideau et al., 2009; Elmo et al., 2018) (Fig. 1 B). Homogeneous disintegrated rock masses tend to exhibit rotational failure and behave as a continuum, similar to a soil (Hoek and Bray, 1981; Eberhardt et al., 2004; Brideau et al., 2009) (Fig. 1 C). While failure mechanisms are key to understanding how individual slopes will fail under various conditions, these concepts are not typically used in regional-scale models of landslide hazard.

Many studies have focused on landslide susceptibility modelling with the aim to predict where coseismic landslides might occur on a regional scale (Jibson, 2011; Reichenbach et al., 2018). Statistics-based susceptibility models typically rely on topographic, hydrologic, and general lithologic factors that are used as proxies for physical parameters influencing landslide susceptibility (Reichenbach et al., 2018). Physics-based models, on the other hand, attempt to predict landslides based on simplified geomechanical models taking into account material strength, topography and ground motion characteristics (Jibson, 2011; Reid et al., 2015; Grant et al., 2016; Pollock et al., 2019). These regional models either assume a specific failure mechanism, which is applied universally, or offer no insight into the mechanism of failure. Neither of these methods provide significant insight into likely volumes. Landslide failure mechanisms and likely volumes, however, are critical for landslide hazard and risk assessments. Moreover, despite the well-known connection between failure mechanism and rock slope stability, little emphasis has been placed on deriving landslide susceptibility factors that are specific to a given failure mechanism for use in regional susceptibility models. This knowledge gap hinders our ability to reliably forecast how landscapes and landslide hazards evolve (e.g. Brain et al., 2021).

To address this gap, we present the results of detailed site-investigations at three landslide sites following the 2016 Mw 7.8 Kaikōura earthquake on the South Island of New Zealand. Based on 3D pixel tracking in pre- and post-earthquake imagery, geomorphic mapping, rock mass characterisation, and geophysical surveys, we develop two conceptual models of failure mechanisms in two different rock types that serve as useful archetypes of c. 70 % of landslides recorded in the 2016 Kaikōura earthquake landslide inventory (Massey et al., 2018b). Based on these two failure mechanisms, we discuss physical processes of initiation that could explain the observed pattern of landslide deformation and link them to relevant landslide susceptibility factors in the different geological settings affected by the Kaikōura earthquake.

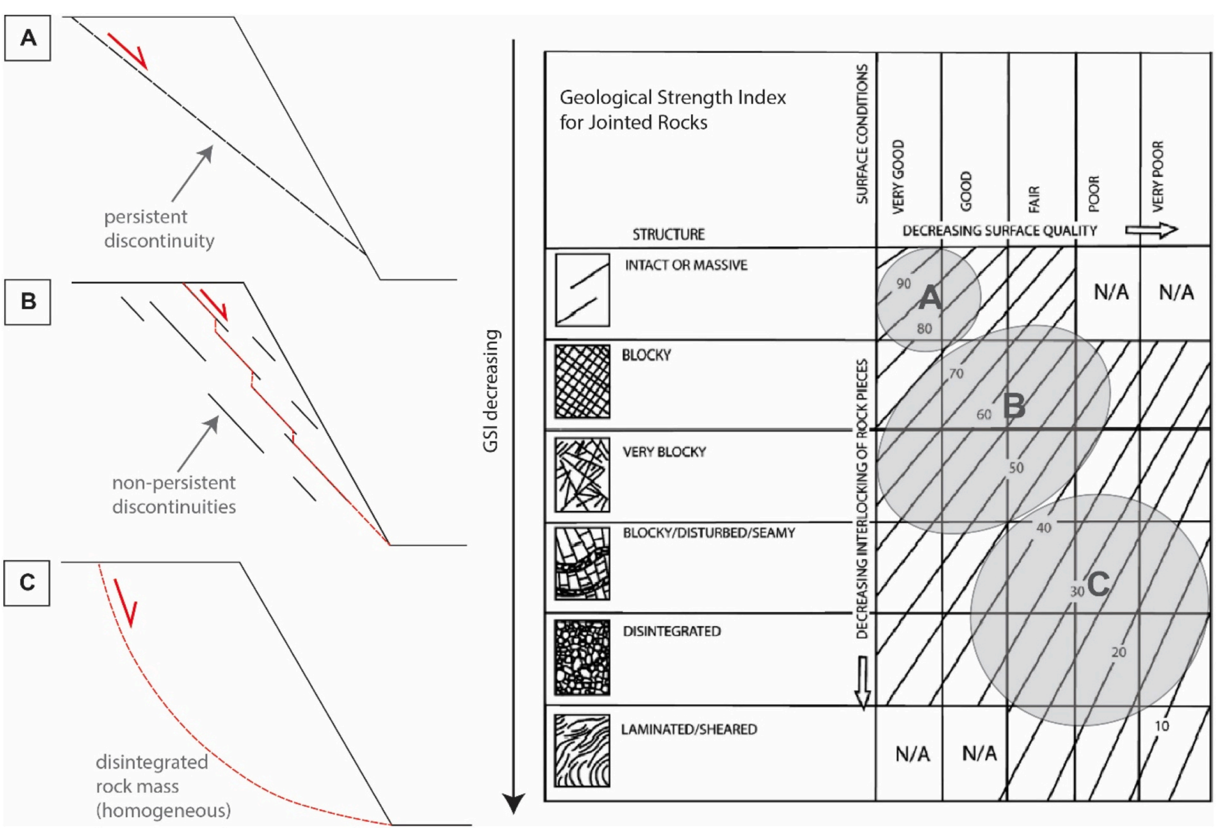

Fig. 1. Typical failure mechanisms are related to the Geological Strength Index (GSI) of rock masses (after Hoek and Marinos, 2000; Eberhardt et al., 2004; Brideau et al., 2009).

2. The 2016 M_w 7.8 Kaikōura earthquake and site geological settings

On November 14th 2016, the Mw 7.8 Kaikōura earthquake caused >20 crustal faults to rupture to the surface (Fig. 2) (Litchfield et al., 2018). Recorded ground motions exceeded 1.0 g horizontal acceleration and up to 2.7 g vertical acceleration (Bradley et al., 2017). As a result, around 30,000 coseismic landslides over an area of about 10,000 km^2 were triggered (Fig. 2) (Dellow et al., 2017; Massey et al., 2018b; Massey et al., 2020a). Based on initial field observations, rock type and structure exerted a strong control over slope failure mechanism during the Kaikōura earthquake (Massey et al., 2018b). Landslides were triggered in four main geological units: Lower Cretaceous basement rocks (predominantly greywacke sandstone and argillite of the Torlesse Supergroup's Pahau Terrane); Upper Cretaceous to Paleogene units (limestone, sandstone, siltstone); Neogene sedimentary rocks (massive but weak limestone, sandstone, and siltstone) and Quaternary sand, silt, and gravel (Massey et al., 2020a). Of the total number of landslides, c. 73 % were located in Cretaceous basement rocks, c. 13 % in Upper Cretaceous to Paleogene units, c. 9 % in Neogene sedimentary rocks, and c. 5 % in Quaternary sand, silt and gravel (Massey et al., 2020a).

In this study, we focus on investigating the failure mechanisms of landslides that occurred in Lower Cretaceous basement rocks and Neogene sedimentary rocks, which respectively compose c. 60 % and 9 % of the surface geologic units in the area affected by coseismic landsliding (Massey et al., 2018b). Torlesse basement rocks predominantly consist of interbedded sandstone and argillite and are loosely referred to as greywacke (Rattenbury et al., 2006). Typically, greywacke is characterised by closely-spaced discontinuity sets (Brideau et al., 2020). Coseismic slope failures in this rock type were mainly rock falls and debris and rock avalanches, with the volume of failure typically limited by the heavily jointed nature of the rock mass (Massey et al., 2018b). Although rare, large-volume landslides that occurred in greywacke slopes were structurally controlled by one or more persistent discontinuities (Massey et al., 2018b).

Neogene sedimentary rocks in the Kaikōura region are typically weak (Uniaxial Compressive Strength <2 MPa), but massive, and failures occurred primarily as slides and rotational failures along bedding planes or other persistent discontinuities (Massey et al., 2018b). A few more weathered portions of the Neogene sedimentary rocks failed as

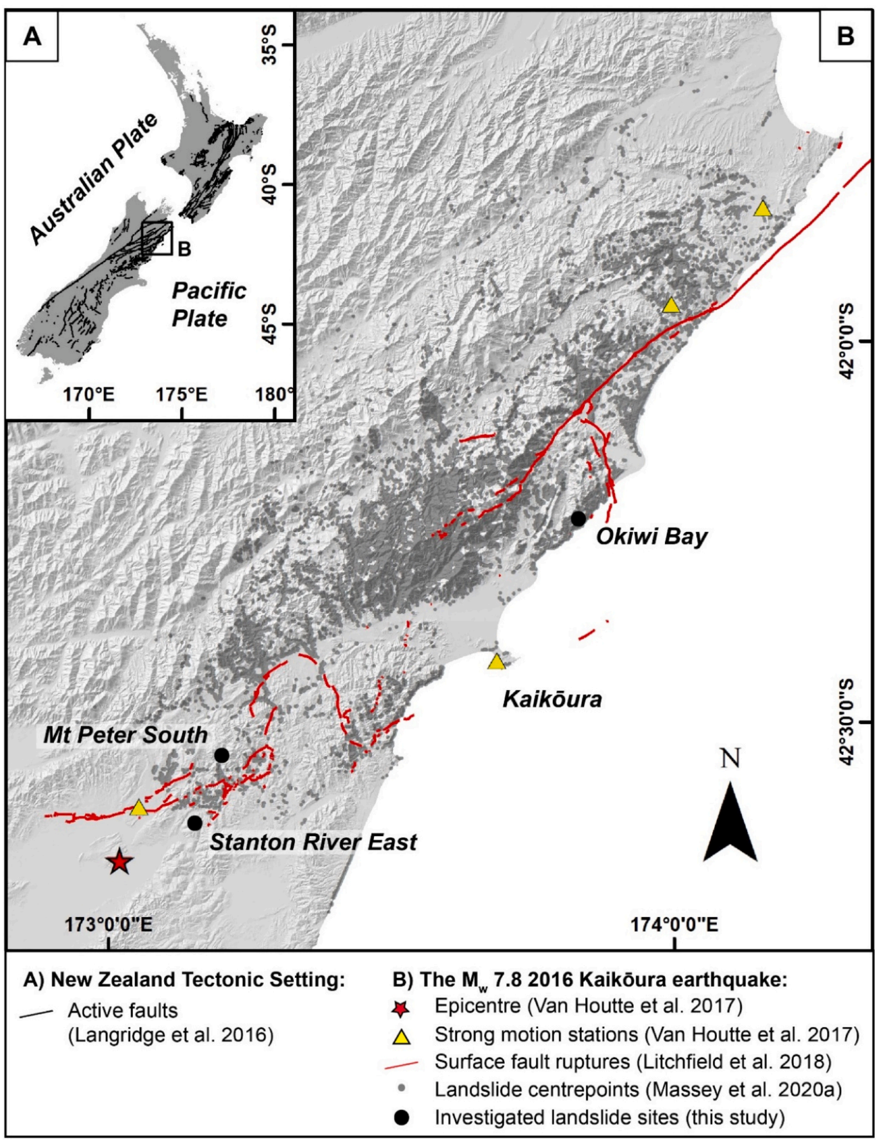

Fig. 2. (A) Tectonic setting and active faults in the New Zealand Active Fault Database (Langridge et al., 2016). (B) Epicentre, strong motion stations and surface fault ruptures of the 2016 Mw 7.8 Kaikōura earthquake (Van Houtte et al., 2017; Litchfield et al., 2018), location of landslides triggered by the 2016 earthquake (Massey et al., 2020a) and study sites.

shallow debris avalanches and flows (Massey et al., 2018b). Many landslides in Neogene sedimentary rocks were reactivated during the 2016 earthquake (Massey et al., 2018b).

We selected two landslides in Torlesse greywacke and one landslide in Neogene siltstone for detailed site-specific analysis (Fig. 2). Since many slope failures in greywacke occurred as debris and rock avalanches with fully evacuated source areas (i.e. no material remains in the source area), few sites preserve evidence of the coseismic failure mechanism (Massey et al., 2020b). As a result, in Torlesse greywacke, we specifically chose an incipient landslide (Okiwi Bay, Fig. 2) and an incipient slide that partially transitioned to a rock avalanche (Mt Peter South, Fig. 2) for our analysis. We also analysed a landslide in Neogene siltstone (Stanton River East, Fig. 2), which is geomorphologically similar to, and representative of, many other failures in this lithology.

3. Data and methods

The three selected landslide sites were characterised using field and remote mapping (geomorphological and structural mapping, rock mass characterisation), 3D pixel tracking in pre- and post-earthquake imagery (Digital Image Correlation and topographic sampling), and geophysical ground investigations (Fig. 3). Results of the different analyses were then interpreted and used to build a conceptual model for each landslide (Fig. 3). The term 'conceptual model' is used in this study to refer to the conceptual engineering geological ground model of an individual landslide. The term 'failure mechanism' is used herein to abstractly describe the type and mechanism of a rock slope failure.

3.1. Aerial photographs and topographic data

Pre- and post-earthquake (i.e. 2015 and 2017) orthophotographs and Digital Surface Models (DSM) produced from digital stereo aerial photographs with a resolution of 0.3 m and 1 m, respectively, were available covering the main area affected by landslides (Massey et al., 2020b). Additionally, 2016 post-event Light Detection and Ranging (LiDAR) and high-resolution orthophotographs (20 cm) were available for analysis (Massey et al., 2018a). These datasets were used as an input for Digital Image Correlation and sampling of pre- and post-earthquake elevation data (i.e. topographic sampling) as well as remote mapping (Fig. 3).

3.2. Field and remote mapping

Landslide geomorphology was mapped in the field and the rock mass structure and quality was characterised for each site (Fig. 3). Joint orientation, roughness, persistence and spacing were described using ISRM (1978) and the Geological Strength Index (GSI) was estimated (Hoek and Brown, 1997). The weathering grades of outcrops were described following Brideau et al. (2020). Pre- and post-event geomorphological mapping was completed using the available orthoimages and Digital Elevation/Surface Models (DEMs/DSMs). Mapped features include ground cracks, scarps, debris trails, breaks in slope, ridgelines, and hydrological features such as streams and drainage channels. Differencing of the DSMs was used to constrain the spatial extents of ground deformation.

3.3. Digital image correlation (DIC) and topographic sampling

Digital Image Correlation (DIC) is an image processing technique that evaluates the internal misalignment of two images using a moving window to compute displacements in line of sight (Bickel et al., 2018). Using this technique, we derived *horizontal coseismic landslide displacements*. Manual feature tracking was used to choose the appropriate window size as well as to validate results obtained through DIC (technical specifications for each site are provided in the Supplementary Information Table S1). Through co-registration of the images during pre-processing in the DIC algorithm, homogeneous horizontal coseismic tectonic displacement at a study site is automatically accounted for.

The *vertical component* of the displacement vector was obtained through topographic sampling of the pre- and post- earthquake Digital Surface Models (DSMs). However, to obtain true vertical landslide displacement, coseismic tectonic displacements needed to be considered. To shift the pre-event DSM into the same reference frame as the post-event DSM, we applied a landslide mask to a three-dimensional tectonic displacement model produced by Howell et al. (2020) using the Iterative Closest Point technique, and determined the average tectonic displacement from the Kaikōura earthquake at each site. This method assumes that tectonic displacement is homogeneous across the site, which is likely valid since the analysis was carried out at a relatively small site-specific scale and the study sites are not located within an area of significant distributed deformation (Zinke et al., 2019; Bloom et al., 2021). We examined the quality of the DSM shift through DSM differencing of the corrected 2015 and the 2017 DSM and found that this method provided a good correlation. Elevation differences in areas without landslide deformation were considerably smaller than the magnitude of landslide displacements (< 1 m).

Based on horizontal and vertical coseismic landslide displacements, full 3D displacement vector fields were derived for each landslide. We then projected the 3D displacements onto profile lines to analyze the pattern of displacement in longitudinal sections parallel to the direction of failure.

3.4. Geophysical surveys

Geophysical surveys were carried out at the Mt. Peter South and Okiwi Bay sites to constrain the landslide geometries and rock mass properties at depth (Fig. 3). Site conditions and topography introduced

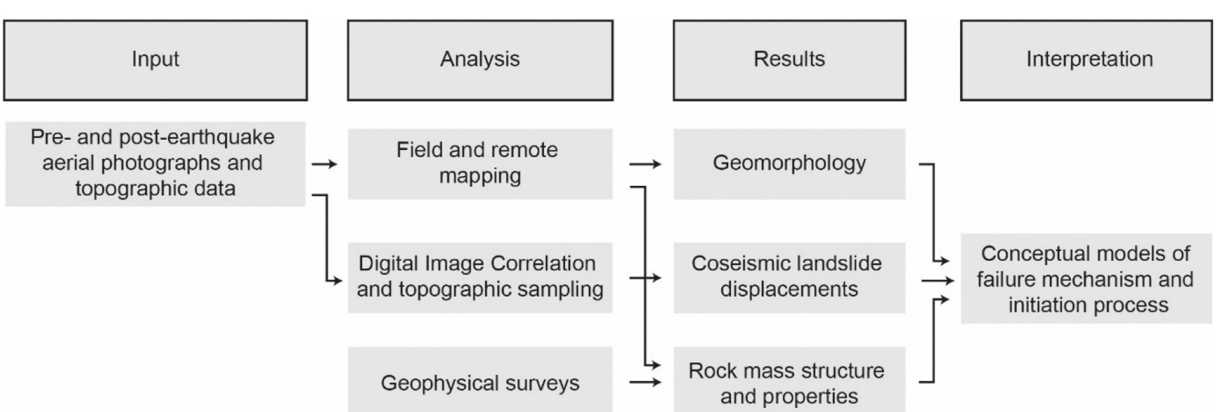

Fig. 3. Workflow and methodology applied in this study.

different challenges for the two techniques used – as a result, we conducted electrical resistivity surveys at Mt. Peter South and seismic surveys at Okiwi Bay. No geophysical surveys were undertaken at Stanton River East where field mapping and remote sensing data were sufficient to construct a conceptual model for the failure.

3.4.1. Electrical resistivity surveys

Electrical resistivity is mainly a function of mineralogy, porosity and ground water content (Archie, 1942). As a result, Electrical Resistivity Tomography (ERT) is useful to gain information on fractures, weathering, groundwater conditions, and water saturation of fractures within a slope (Heincke et al., 2010). It has been successfully applied in landslide investigations to reconstruct landslide depth and geometry (Perrone et al., 2014). In this study, we conducted two ERT surveys at the Mt. Peter South site to investigate the internal structure of the partially failed landslide. The two ERT surveys were carried out using an Iris Syscal resistivity meter using a 2.5 m electrode spacing along 240 m profiles. Data were collected using Wenner-α and Dipole-Dipole electrode geometries. The locations of points along each survey line were recorded using a handheld Garmin GPS and elevation data were extracted from the 2016 LiDAR DEM. We displayed the recorded data in pseudosections to verify the geometry and remove anomalous data and then inverted the 2D resistivity data with topography using the inversion software Res2Dinv (Loke and Dahlin, 2002).

3.4.2. Seismic surveys

Seismic Refraction Tomography (SRT) is commonly used on landslides to carry out subsurface mapping of discontinuities, obtain bulk rock mass properties, identify zones with high fracture density, and derive the depth of the landslide (Heincke et al., 2006; Heincke et al., 2010; Cody et al., 2019). Furthermore, multi-channel analysis of surface waves (MASW) can be used to obtain 1D profiles of shear wave velocities (Park et al., 1999) and is suitable for near-surface geotechnical characterisation (Duffy, 2008; Pazzi et al., 2019; Whiteley et al., 2019). The combination of SRT and MASW can be very useful in identifying changes in water saturation and elastic properties of the rock.

Two SRT surveys with 24 geophones at 4 m spacing were carried out along a vehicle track crossing the Okiwi Bay site perpendicular to the failure direction. Seismic waves were created using a 20 lb. sledgehammer. A minimum of three shots were stacked to increase the signal-to-noise ratio. The geometry of the geophone array and shot locations is provided in the Supplementary Information, Fig. S1. The locations of the geophone array and all source positions were recorded using a Trimble Geo7x GNSS receiver. The seismic refraction data were processed using Reflex W 7.0 (Sandmeier, 2012). Picking of first arrivals was carried out manually in Reflex W. Tomographic results were then obtained through two-dimensional (2D) inversion of the travel times for the first arrivals in Reflex W. Ray path tracing was performed to understand the ray coverage within the model cells, and those cells with low coverage were masked because they were poorly resolved.

Additionally, a MASW survey using a 24-channel landstreamer with 2 m geophone spacing was carried out along the same vehicle track crossing the Okiwi Bay site perpendicular to the failure direction. Spacing between shots varied between 5 m and 30 m along the transect due to topographic constraints. Seismic surface waves were generated using a 20 lb. sledgehammer. A minimum of three shots were stacked to increase the signal-to-noise ratio. The shot locations were offset by 10 m from the MASW array and the midpoint of the geophone array was recorded for each shot location using a Trimble Geo7x GNSS receiver. The MASW data were processed using SurfSeis 6 (Kansas Geological Survey, 2018). The surface waves showed significant dispersion across the array. We manually picked dispersion curves for each array and preformed a one-dimensional (1D) inversion of the curve in SurfSeis. The resulting 1D shear-wave velocity profiles and Root-Mean-Square Errors (RMSE) of each v_s value were interpolated along a 2D profile in MATLAB using a triangulation-based natural neighbor algorithm.

3.5. Conceptual models

The results of Digital Image Correlation and topographic sampling, field and remote mapping, and geophysical surveys were integrated to develop conceptual models of each landslide (Fig. 3). Landslide surface displacements as well as discontinuity data, geomorphology and, where available, geophysical survey results were used to reconstruct the shape of the rupture surface and interpret the failure mechanism at each site.

4. Site-specific results and interpretation

4.1. Mt. Peter South landslide

The Mount Peter South landslide is located in the hills of North Canterbury (Fig. 2) in Torlesse greywacke rock mass. This landslide partially mobilised during the 2016 Mw 7.8 Kaikōura earthquake (Fig. 4A). The upper portion of the slope exhibits ground deformation thought to represent incipient sliding while the lower portion of the landslide transitioned into a debris avalanche during the 2016 earthquake.

4.1.1. Geomorphology

The hillslope on which the Mt. Peter South landslide occured has a slope of c. 28 to 35° and ranges in elevation between 520 m.a.s.l. and 750 m.a.s.l. The head scarp of the incipient landslide is located close to the ridgeline and the debris trail of the avalanche extends to the valley bottom. The northern lateral boundary of the landslide is clearly marked by a lateral scarp, whereas the southeastern lateral boundary is expressed diffusely through minor bulging. The incipient portion of the landslide can be divided into three deformation domains based on predominantly translational, compressional, and extensional morphological surface features (Fig. 4B). The translational domain is bounded by the head scarp and a concave break in slope. Multiple translational sub-domains were mapped, which show relatively little internal deformation and are typically delineated by scarps and tension cracks. The occurrence of tension cracks within the translational domain indicates that some extension occurs in this domain. However, since the extensional deformation in this domain is mainly concentrated in zones between translational sub-domains, we refer to it herein as the translational domain. The compressional domain is characterised by counter scarps and bulging and is found in a zone of the slope with comparatively low slope angles. Further downslope, slope angles become steeper and tension cracking is abundant – this domain is therefore described as the extensional domain (even though, to a lesser extent, translation also occurs).

Pre-earthquake geomorphology observed on the 2015 DSM suggests that a relict landslide is located in the southern part of the hillslope (Fig. 4B). Even though the extent of the 2016 coseismic landslide and the relict landslide are not identical, it is likely that the occurrence of the 2016 coseismic landslide was influenced by the pre-existing landslide (i.e. representing an enlargement of the relict landslide). Here, however, we focus on the well-constrained coseismic deformation of the slope.

4.1.2. Coseismic landslide displacements

Digital Image Correlation (DIC) and topographic sampling of the Mt. Peter South landslide pre- and post-earthquake shows an average of 6.4 m 3D coseismic landslide displacement (Fig. 4C). Maximum 3D displacements of up to 12.3 m are found in the central portion of the slope. In areas with debris cover and high ground disturbance (i.e. cracks), the images cannot be correlated using DIC. Maximum horizontal displacements from manual feature tracking in the central portion of the landslide reach up to 15.4 m.

In the northern portion of the landslide the magnitude of displacement downslope of the head scarp stays relatively constant at c. 8 m (Fig. 4C and D, Profile 1). Ground cracking observed between c. 10–40 m along profile 1 can be associated with the head scarp. No major ground

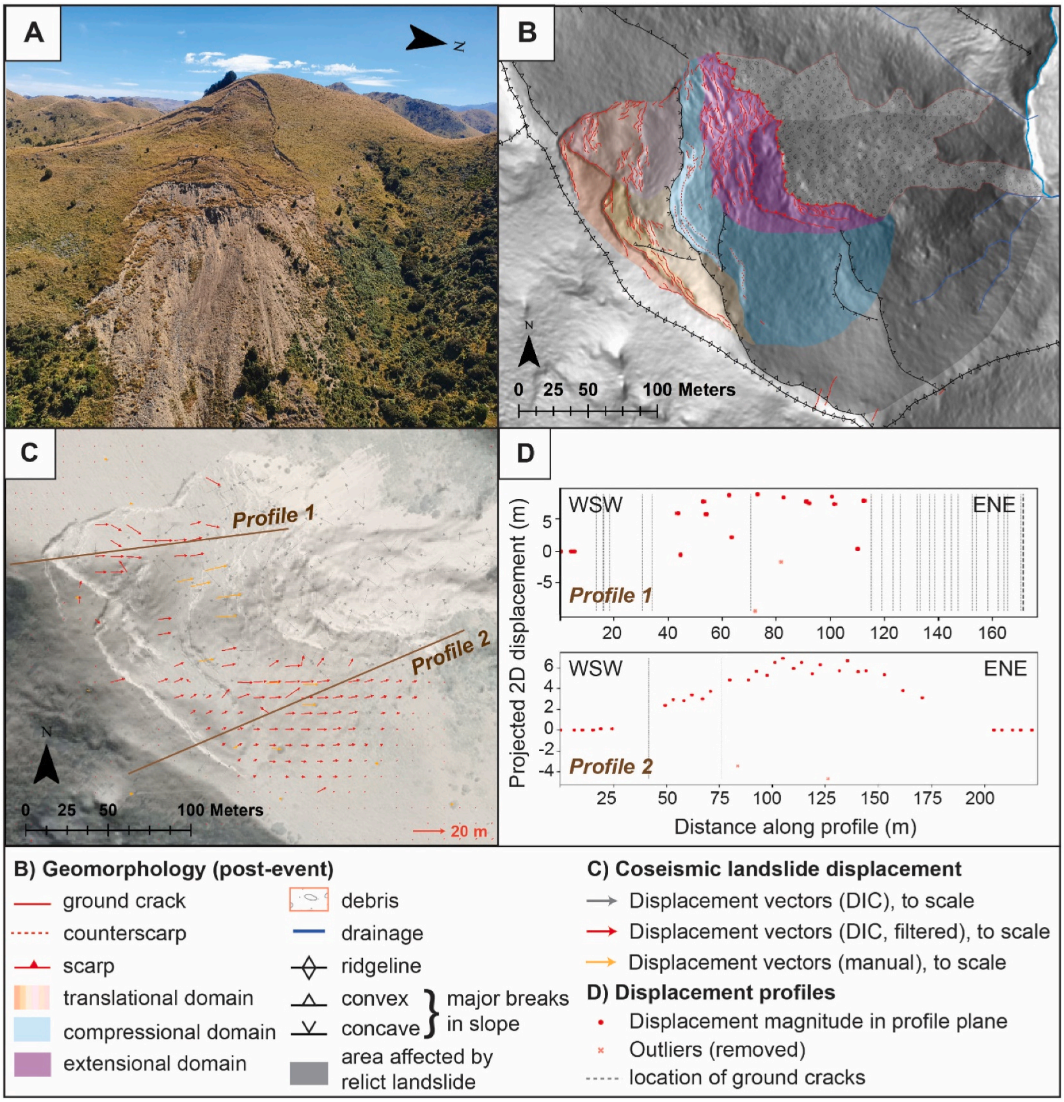

Fig. 4. Mt. Peter South landslide in North Canterbury (A) and mapped geomorphology (B) based on the post-earthquake 2016 DEM. Coseismic horizontal displacement vectors were projected on to two longitudinal profiles (C) and plotted in (D).

cracking is observed between c. 40–110 m along profile 1, where displacements stay relatively constant. From c. 110 m along profile 1, a high density of tension cracks in the extensional domain prevents displacement measurements using DIC (Fig. 4D).

In the southern portion of the landslide (Fig. 4C and D, Profile 2) the magnitude of displacement gradually increases below the head scarp of the landslide (c. 40–100 m along profile 2) and reaches a maximum displacement of c. 6 m (c. 100–150 m along profile 2). Two zones of ground cracking (at c. 40 m and 75 m) can be observed in this part of the profile, which can be associated with the head scarp and a counterscarp, respectively. Subsequently, displacement magnitudes decrease towards the diffuse southeastern lateral boundary of the landslide (c. 150–200 m along profile 2) without any ground cracking occurring.

4.1.3. *Rock mass structure and properties*

Greywacke rock mass is exposed in outcrops along the head scarp and in ground cracks within the landslide as well as in several places outside the area affected by the landslide. The rock mass consists of closely jointed moderately to highly weathered sandstone. While not observed in any of the outcrops in and around the landslide, bedding dips steeply towards the west in this region (Supplementary Information, Fig. S2). Four main joint sets (JS1–4) with m-scale persistence were identified by structural measurements collected along the head scarp of the landslide and in outcrops just outside of the landslide extent (Supplementary Information: Table S2). Small-scale fractures (c. 1–20 cm persistence) were observed in abundance in these outcrops but are highly variable in orientation, and are thus considered to be randomly oriented. In outcrops within the landslide (i.e. head scarp, tension cracks, and counter scarps), GSI estimates range from 30 to 40 (Supplementary Information, Fig. S3). Outside the landslide, outcrop GSI ranges from 45 to 55 (Supplementary Information, Fig. S3).

The two Electrical Resistivity Tomography (ERT) surveys conducted at Mt. Peter South using both Dipole-Dipole (Fig. 5) and Wenner-α acquisition (Supplementary Information, Fig. S4) indicate the variability of rock mass properties with depth and allow us to interpret landslide depth. These interpretations are based on the hypothesis that intact greywacke is resistive. Fracturing increases porosity and, thus, if fractures in greywacke are unsaturated and do not contain clay, resistivity increases (i.e. the ability of the rock to conduct electricity decreases). If clay fracture infills are present due to weathering of the rock mass or the rock mass is saturated, resistivity will decrease.

In the longitudinal section (Fig. 5B), a 5-m-thick zone of high resistivity can be observed along the ridge crest (c. 0–45 m along profile). This section of the profile is located outside of the landslide and the high

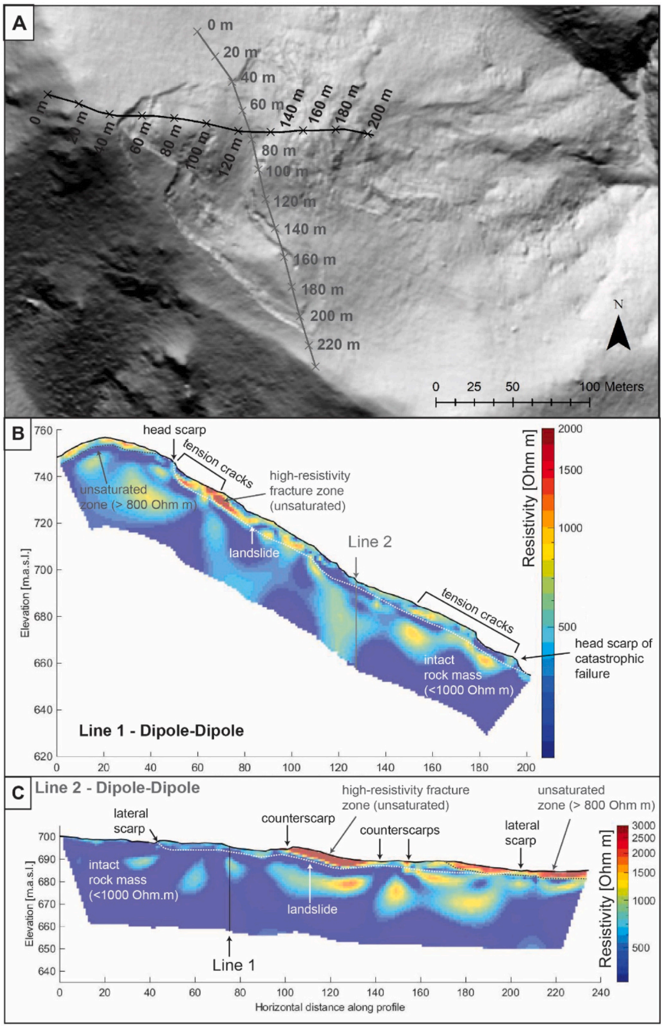

Fig. 5. Location of ERT transects at the Mt. Peter South landslide (A). Longitudinal profile is black and the transverse profile is grey. The sections are presented in (B) longitudinal and (C) transverse (C) resistivity sections annotated with geomorphological features and interpretations.

resistivity zone (> 800 Ohm m) likely represents unsaturated and in-situ but fractured rock or soil. Downslope of the head scarp (c. 50–70 m along profile), a very high resistivity zone from 0 m - c. 10 m depth can be observed (Fig. 5B). This zone corresponds to an area with a high density of tension cracks that mark the upper end of the translational domain at the surface (Fig. 4B). A resistivity of >1500 Ohm m can be explained by the high porosity in the head scarp and tension cracks provided the area is unsaturated. We therefore interpret the sharp resistivity contrast at c. 10 m depth as the landslide base. Below the landslide base, an increase in saturation or drop in porosity may increase electrical conductivity in the intact rock mass, reducing the resistivity to <500 Ohm m. Further downslope (c. 70 m – 110 m along profile), a contrast between high resistivity (500–1000 Ohm m) at depths shallower than c. 10–15 m and lower resistivity (< 500 Ohm m) at greater depths remains, but is less stark than farther upslope (Fig. 5B). This resistivity contrast could indicate that the shallow material in this part of the translational domain remained more intact, but some rock mass damage and resulting increased porosity are associated with the basal failure zone. As such, we interpret that landslide depth in this part of the slope is located at c. 10 m depth.

Between c. 110 m – 150 m along profile (Fig. 5B), resistivity is generally low and no sharp contact with the underlying geology can be seen. This part of the profile corresponds to a concave break in slope and the transition between the translational and compressional domains at the surface (c. 127 m along profile). In this part of the slope saturation conditions possibly change due to the concave break in slope. Furthermore, compressional deformation could lead to a decrease of porosity and, hence, lower resistivity. As a result, landslide depths in this part of the slope are poorly constrained. In the extensional geomorphological domain (> 150 m along profile), resistivity at depths c. < 10 m are moderate to high (500–1000 Ohm m) based on the Dipole-Dipole acquisition results (Fig. 5B). In the results of the Wenner-α acquisition, however, a resistivity contrast at c. 5–10 m is apparent in this part of the profile (Supplementary Information, Fig. S3). High resistivity values in this part of the slope could be related to the high density of tension cracks in unsaturated conditions. However, Dipole-Dipole results would be expected to be more sensitive to discrete fractures than Wenner-α results. The difference in resistivity results between the two acquisition protocols and the end-of-line location therefore suggest that measurement uncertainties are high. With some uncertainty, landslide depth in the extensional domain can be estimated to c. 10 m depth. All along the longitudinal section (Fig. 5B), some variability in resistivity can be observed below depths of c. 10–15 m. This is likely related to lithological variability (i.e. argillite and sandstone beds) as resistivity contrasts are sub-vertical and bedding at the site is dipping steeply to the west (Supplementary Information, Fig. S2).

The transverse section (Fig. 5C) crosscuts the translational and compressional domains of the landslide (Fig. 4B). At the mapped lateral scarp of the landslide (c. 40 m along profile), an increase in resistivity of c. 10 m depth is observed. This resistivity contrast can be traced between c. 40 and 100 m along profile at c. 10 m depth (Fig. 5C). This section of the profile corresponds to the translational domain and, similar to the longitudinal profile, the resistivity contrast can be explained by increased porosity in unsaturated conditions. The base of the high resistivity zone is interpreted to be the base of the landslide. At c. 100 m and c. 140 m along profile, sharp resistivity contrasts each coincide with the counterscarp that marks the transition between the translational and compressional domain (Fig. 5C). Very high resistivity of c. 10 m depth and a sharp horizontal contrast can be observed in the compressional domain (c. 100–140 m along profile). This very high resistivity zone (> 1500 Ohm m) is likely related to the counterscarp causing locally very high porosity in unsaturated conditions. A c. 5-m-deep high resistivity zone continues in the translational domain (c. 140–200 m along profile) and beyond the lateral scarp of the landslide (> 200 m along profile). The depth of the landslide in this section along the profile can be interpreted to about 5–10 m depth. In the field, a shallow layer of colluvium (c. 1 m thick) possibly related to the relict landslide present in this part of the slope was observed in this area, which could explain the continuation of a c. 5-m-deep high resistivity zone south of the lateral scarp of the landslide. Zones of high resistivity at depths greater than the interpreted landslide base (i.e. > 10–15 m) are present in the southern part of the profile (c. 100–220 m). These zones could be related to saturation conditions or local variabilities in rock mass properties (Fig. 4B).

4.1.4. *Conceptual model and interpretation of failure mechanism*

At the Mt. Peter South site, the observed displacement patterns correlate well with the interpreted geomorphological deformation domains (Fig. 4B and C). The translational domains are characterised by constant displacements and relatively little internal deformation. The compressional domain shows a downslope decrease of displacement magnitude. Some distinct counterscarps were mapped, which accommodate parts of the deformation resulting from the displacement gradient. The remaining compressional deformation is accounted for by distributed rock mass deformation and expressed through bulging. The extensional domain shows a downslope increase in displacement magnitudes accommodated by an increased density of tension cracks. The incipient deformation of the slope (i.e. transitional and compressional domain) thus resembles a 'Prandtl mechanism' which is defined by the upper part of the slope actively driving the failure leading compressive deformation to accumulate in the lower, passive portion of the slope (Kvapil and Clews, 1979). The boundary between the translational and compressive domain thus represents the transition between the active and passive deformation of the slope and is geomorphologically expressed by counterscarps. Based on these observations, we hypothesise that the failure initiated in the upper part of the slope.

In the active upper portion of the Mt. Peter South landslide, the steeply dipping joint set, JS1, is favourably oriented for failure and likely influences the stability of the slope. The dip of displacement vectors in this part of the slope also coincides with the dip of JS1 (Fig. 6), which suggests that the rupture plane developed along defects of JS1. That said, JS1 has a limited persistence (c. 2.0 m) and the geometry of the landslide at depth (Fig. 5) cannot be geometrically explained by a simple structurally controlled failure mechanism. Furthermore, the surface morphology of the landslide also suggests a more complex rupture geometry. A step-path failure mechanism with the rupture plane propagating along cm-scale discontinuities between more persistent defects better explains the failure mechanism (Fig. 6). This deviates slightly from the step-path failure mechanism described in literature (Fig. 1) as, in the greywacke rock mass, the closely jointed nature of the rock mass enables rupture plane propagation along small-scale discontinuities without the breaking of intact rock bridges. This hypothesis is supported by laboratory tests of fractured core by Brideau et al. (2020), in which most samples failed along pre-existing discontinuities.

4.2. *Okiwi Bay incipient landslide*

The Okiwi Bay site is located along the coast north of the township of Kaikōura (Fig. 2). During the 2016 Kaikōura earthquake, an incipient landslide caused ground deformation in the greywacke rock mass (Fig. 7A).

4.2.1. *Geomorphology*

The Okiwi Bay incipient rock slide is located in the upper part of a coastal hillslope with slope angles ranging between 35° and 55° at elevations ranging from 10 m.a.s.l. to 220 m.a.s.l. Coseismic displacement of the landslide is expressed through tension cracks in the upper portion of the slope (Fig. 7B). Observations of pre-earthquake geomorphology (2015 DSM) reveal that scarps along the ridge crest (i.e. above the main area of coseismic deformation) were present before the 2016 earthquake. Tension cracks along these scarps were observed after the earthquake, but displacement magnitudes were small (<1 m). The toe of the landslide is located at a concave break in slope around 90 m.a.s.l. (Fig. 7B). Laterally, coseismic landslide deformation is limited to a 'knob-like' topographic feature (Fig. 7B and C) and the areas with coseismic displacement are characterised by a higher surface roughness as compared to the rest of the hillslope.

4.2.2. *Coseismic landslide displacements*

The extent of coseismic displacement identified through differencing of the pre- and post-earthquake DSMs (i.e. translational and compressional domain) is bound to the upper central part of the slope (Fig. 7B). Digital Image Correlation (DIC) and topographic sampling of the pre- and post-earthquake DSM reveal coseismic landslide displacements of >1 m c. 40 m away from the ridge crest (Fig. 7C). Displacement along minor tension cracks (< 1 m) closer to the ridge crest could not be resolved using the applied techniques. We therefore use the term 'area of main coseismic deformation' to describe the spatial extent of displacements >1 m. Displacements increase downslope reaching values of up to 9.8 m (3D) in the central part of the slope and subsequently decrease to <1 m at about 220 m horizontal distance from the slope crest. This 'bell-shaped' displacement pattern is also apparent in profile view of the projected landslide displacement vectors (Fig. 7D). The increase of displacement magnitudes in the upper portion of the slope can be correlated with mapped ground cracks (<130 m along profile), whereas no ground cracks were mapped farther downslope where displacement magnitudes gradually decrease (Fig. 7D).

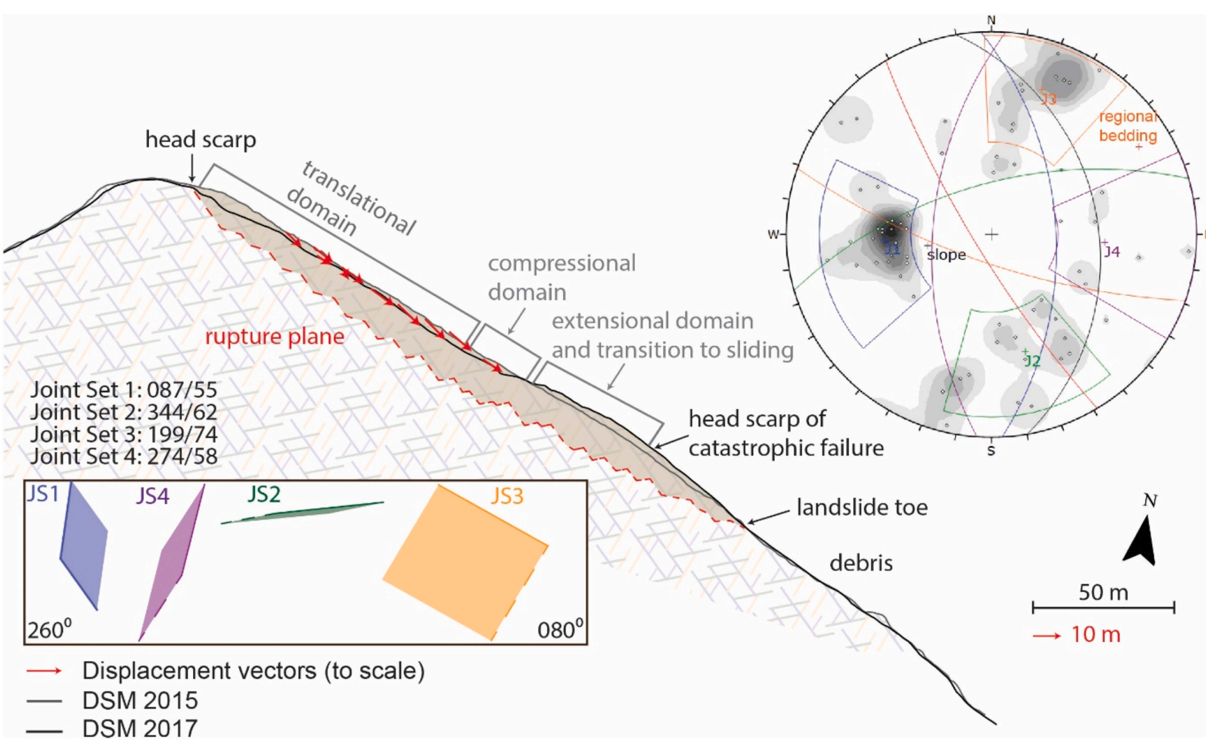

Fig. 6. Conceptual model of the joint-step-path failure mechanism at Mt. Peter South and stereoplot of joint measurements taken in the field. Orientations of joint sets are given as (dip direction/dip), stereonet contours vary from 0 % to 14 %, intervals are 1.4 % as defined by a Fisher distribution (Fisher, 1953).

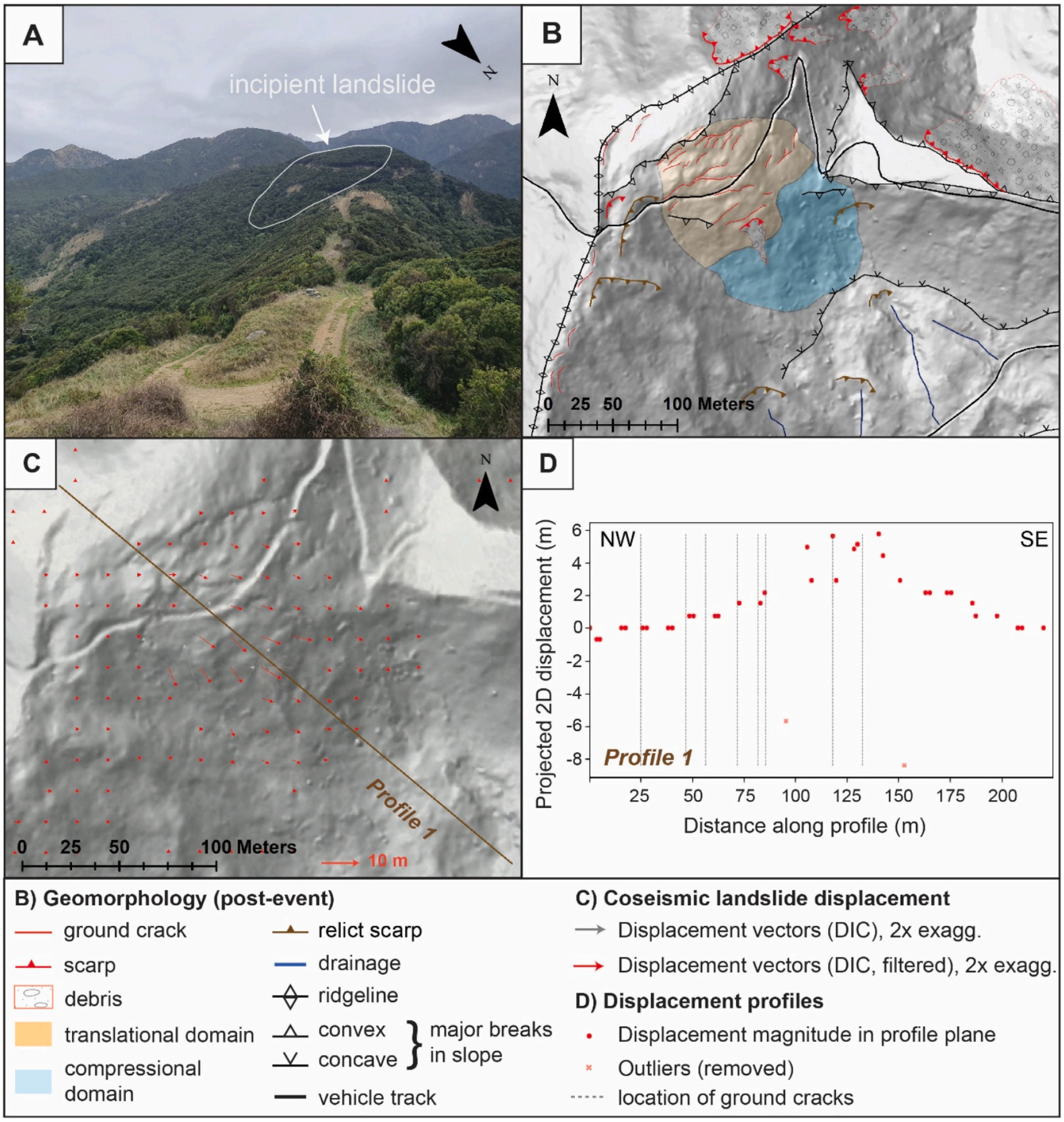

Fig. 7. Okiwi Bay incipient landslide on the coast North of Kaikōura (A) and mapped geomorphology (B) based on the post-earthquake 2016 DEM. Coseismic horizontal displacement vectors were projected on to a longitudinal profile (C) and plotted in (D).

4.2.3. *Rock mass structure and properties*

Greywacke rock mass is exposed along a vehicle track that crosses the central portion of the incipient landslide perpendicular to the direction of failure. Local lithology within the Torlesse greywacke is predominantly massive sandstone with some c. 0.5–1 m thick argillite beds that make up the most heavily weathered zones in outcrop (bedding orientation: 244/43). Outcrops are heavily fractured and moderately to highly weathered. Five main joint sets (JS1–5) with m-scale persistence were identified based on structural measurements in the field (Supplementary Information: Table S3). Similar to the Mt. Peter South landslide, small-scale fractures (c. 1–20 cm persistence) are abundant, but highly variable in orientation. Estimates of GSI in outcrops along the vehicle track crossing the landslide range from 30 to 50 (Supplementary Information, Fig. S3). An overview of the regional geology at the Okiwi Bay site is provided in the Supplementary Information, Fig. S2.

Seismic velocities in transects across the incipient landslide vary between 200 m/s and 1000 m/s (S-wave velocity: v_s), and 700 m/s and 1600 m/s (P-wave velocity: v_p) (Fig. 8). The velocities generally increase with depth, but a concave-up shaped zone of high velocity gradient indicates a material interface in the S-wave velocity profile (MASW: v_s) with a maximum depth of c. 35 m below ground surface (Fig. 8C). Since no geological contacts were observed in the landslide mass, this material interface likely represents a change in fracture intensity, and we interpret this interface as the base of the incipient landslide. The same pattern is observed in P-wave velocities but is less apparent due to a lack of penetration of the ray-paths in the central part of the profile that is caused by the overlap of the two seismic refraction profiles. Laboratory testing of Torlesse greywacke samples from the Wellington region (similar rock type as described at Okiwi Bay) by Brideau et al. (2020) showed S-wave velocities of 800–3300 m/s and P-wave velocities of 1600 m/s - 5500 m/s with variability attributed to weathering and the number of discontinuities. Comparatively, S-wave velocities measured in the MASW transect within the landslide at Okiwi Bay are 200–600 m/s, c. 25–93 % lower than measured at core-scale in the laboratory. Outside the landslide, S-wave velocities in the MASW transect were 400–1000 m/s, c. 0–87 % lower than the measured cores. P-wave velocities within the landslide are <1200 m/s (25 % - 96 % lower) and outside the landslide are 700–1600 m/s (0–87 % lower than in the laboratory). The lower velocities within the landslide suggest that the rock mass is heavily damaged and fractured, in part, due to incipient sliding.

4.2.4. *Conceptual model and interpretation of failure mechanism*

The analysis of coseismic landslide displacements, as well as the

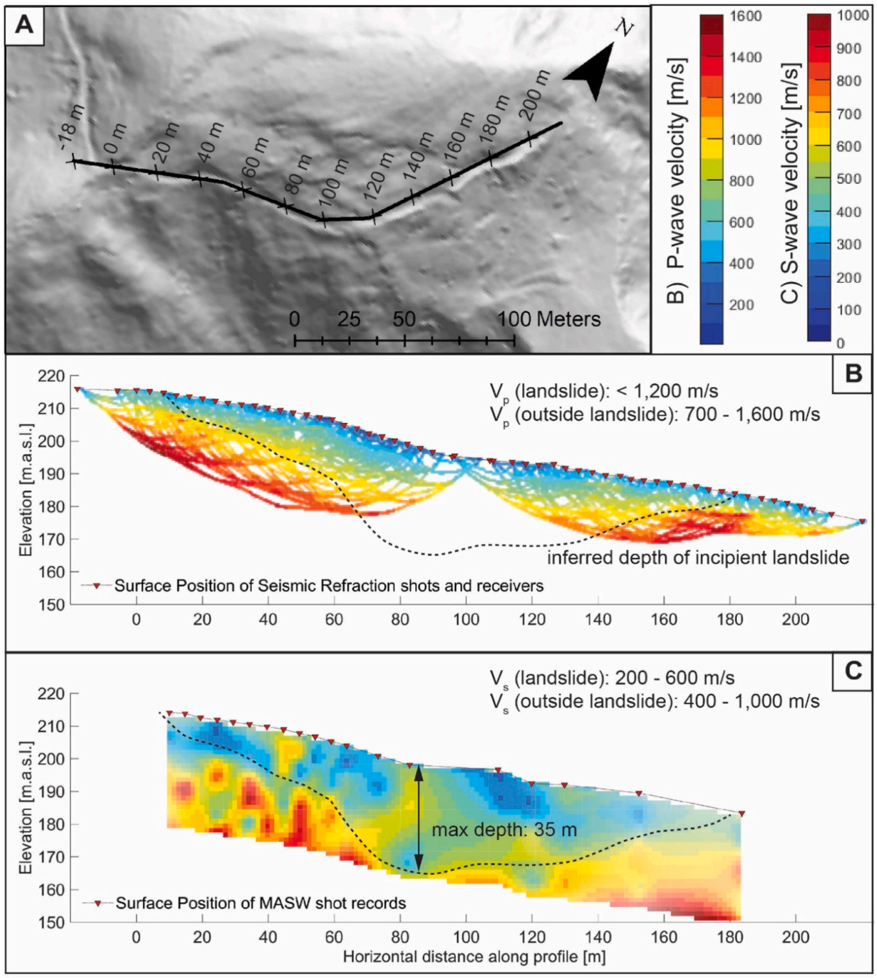

Fig. 8. Location of seismic surveys at the Okiwi Bay landslide (A), P-wave (B), and S-wave (C) velocity profile annotated with velocity ranges and interpreted landslide depth.

results of the geophysical surveys, allowed us to delineate the extent of the Okiwi Bay incipient landslide. Based on displacement results, the coseismic deformation is limited to a knob-like topographic feature with increased surface roughness (Fig. 7B). Results of the seismic surveys indicate a wedge-shaped base with a maximum depth of c. 35 m (Fig. 8). Based on the location of the head scarp, landslide toe, and the landslide depth identified from the seismic survey, the shape of landslide base is well constrained and quasi-planar (Fig. 9).

The displacement pattern with its distinct 'bell-shaped' curve correlates well with observed geomorphic deformation features in the slope (Fig. 7B and D). Tension cracks mark the head scarp of the coseismic deformation and coincide with displacement magnitude increases in the upper part of the slope (Fig. 7D). Extensional and translational deformation is thus predominant in that part of the slope. To be consistent with the terminology used at the Mt. Peter South site, we describe the deformation domain associated with translation and extension as the translational domain (Fig. 7B). The decrease of displacement magnitudes in the lower part of the slope, on the other hand, is associated with compressional deformation. The displacement gradient in the compressional domain is likely accommodated by distributed rock mass deformation since no discrete geomorphological evidence of compressional deformation has been mapped. However, due to extremely dense vegetation and limited accessibility, the absence of discrete compressional geomorphological features could not be verified in the field.

Several m-scale joint sets have been identified that could affect the stability of the site (Fig. 9) but bedding is unlikely to influence slope behavior (i.e. sliding influenced by argillite beds is not kinematically feasible due to bedding being oriented perpendicular to the slope) (Supplementary Information, Fig. S2). One of the dominant joint sets, JS3, with a mean persistence of c. 0.9 m is favourably oriented for failure and likely influences slope stability. However, like the Mt. Peter South site, based on the orientation of m-scaled joint sets, the estimated shape of the landslide base cannot be geometrically explained by a simple structurally controlled failure mechanism. The close spacing and low persistence of joints, high variability of joint orientations, and abundance of cm-scale discontinuities leads to multiple degrees of kinematic freedom in the rock mass. As such, we interpret the failure mechanism of this landslide to also be a joint-step-path failure partially facilitated by m-scale discontinuities and propagation of the rupture plane along cm-scale joints (Fig. 9). Based on the spatial variation of displacement vector dip and magnitudes, along with the surface morphology caused by the movement of the landslide and the shape of the landslide base, we suggest that the upper portion of the slope (i.e. translational domain) was actively driving the deformation of the lower portion of the slope (i.e. compressional domain). The mechanism of deformation thus resembles the Prandtl mechanism and we hypothesise that the rupture plane initiated close to the ridge crest and propagated towards the landslide toe.

Based on pre-earthquake geomorphology that shows relict scarps above the area of main coseismic deformation, we suggest that the Okiwi Bay landslide likely initiated prior to the 2016 Kaikōura event. Furthermore, despite coseismic displacements of c. 3 m at the location of

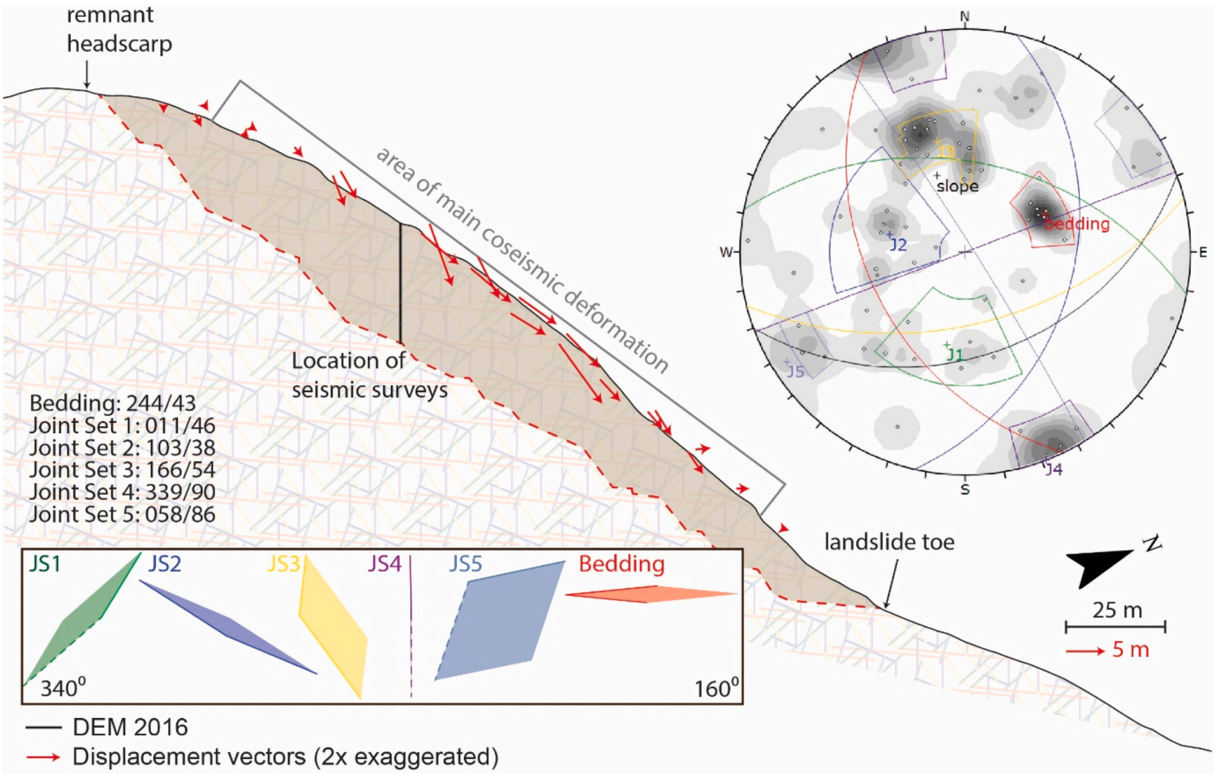

Fig. 9. Conceptual model of the joint-step-path failure mechanism at Okiwi Bay and stereoplot of joint measurements taken in the field. Orientations of joint sets are given as (dip direction/dip), stereonet contours vary from 0 % to 10 %, intervals are 1.0 % as defined by a Fisher distribution (Fisher, 1953).

the seismic transects, very low seismic velocities suggest a high degree of rock mass fracturing (Fig. 8), which is not readily explained by rock mass damage from a single earthquake event. Moreover, the high variability of joint orientations, low mean persistence (c. 0.5–1.1 m) and close spacing of joint sets reflect the heavily deformed and damaged nature of the rock mass at Okiwi Bay that is likely developed over multiple earthquakes (Parker et al., 2015), possibly within the fault damage zone of the Hope fault (e.g., Bloom et al., 2021).

4.3. Stanton River East landslide

The Stanton River East landslide is located in North Canterbury (Fig. 2) adjacent to the terraces of the Stanton River, and failed in Greta Formation Neogene siltstone (Fig. 10A).

4.3.1. Geomorphology

The landslide has a clearly defined head scarp with a c. 60 m wide zone of intense tension cracking beneath the head scarp (Fig. 10B). Ground cracking was observed above the main head scarp in the northern portion of the landslide along a pre-existing arcuate break in slope. The toe of the landslide is located at the valley bottom near the riverbed of the Stanton River (Fig. 10A). The southern portion of the landslide toe is marked by bulging as the landslide displaced formerly flat-lying modern river terrace material. In the northern portion of the landslide toe, where the river was actively eroding a steep outcrop of Neogene siltstone prior to the earthquake, secondary rotational failures of the displaced landslide material can be observed. The northern lateral boundary of the landslide is located in an East-West oriented gully, where landslide debris was observed overriding bedrock within a small stream (Fig. 10B).

4.3.2. Coseismic landslide displacements

At the Stanton River East landslide, coseismic landslide displacements based on DIC and topographic sampling are coherent in direction and magnitude throughout the main body of the landslide with an average displacement of 16.8 m towards the northwest (Fig. 10C). This displacement pattern is also apparent in profile view (Fig. 10D) with most of the displacement accommodated along the main head scarp. In Profile 1 (Fig. 10D), minor displacement (< 1 m) above the main landslide scarp were measured and some displacement occurs along tension cracks at 150–200 m profile distance. In Profile 2 (Fig. 10D), most of the displacement is accommodated along the main landslide head scarp with some displacement occurring in tension cracks at c. 220–250 m along profile. High ground disturbance and debris cover limited measurements of displacement close to the toe of the landslide.

4.3.3. Rock mass structure and properties

The rock mass consists of Greta Formation massive siltstone with some interbedded sandstone (Rattenbury et al., 2006, and this study), and has a GSI of 75–80. Bedding is consistent and dips shallowly (16°-20°) towards the northwest (Supplementary Information, Fig. S2).

4.3.4. Conceptual model and interpretation of failure mechanism

The Stanton River East landslide differs from the two previously described landslides. The displacement is homogeneous in the main landslide body indicating coherent displacement. Ground cracks close to the head scarp indicate extension associated with the translation of the main landslide body. Due to predominantly translational deformation, we describe this domain associated with translation and extension along the head scarp as the translational domain. The debris-covered landslide toe shows signs of bulging and is thus mapped as a compressional domain even though, to a lesser extent, secondary slumping can be observed. The dip and orientation of displacement vectors closely corresponds to the orientation of bedding (Fig. 11) and only deviates from this trend in the area of the head scarp and toe. Based on geomorphology, displacement data, and bedrock structure, this landslide can be classified as a bedding-controlled planar translational rockslide (Hungr et al., 2013). Based on pre-earthquake geomorphology observed

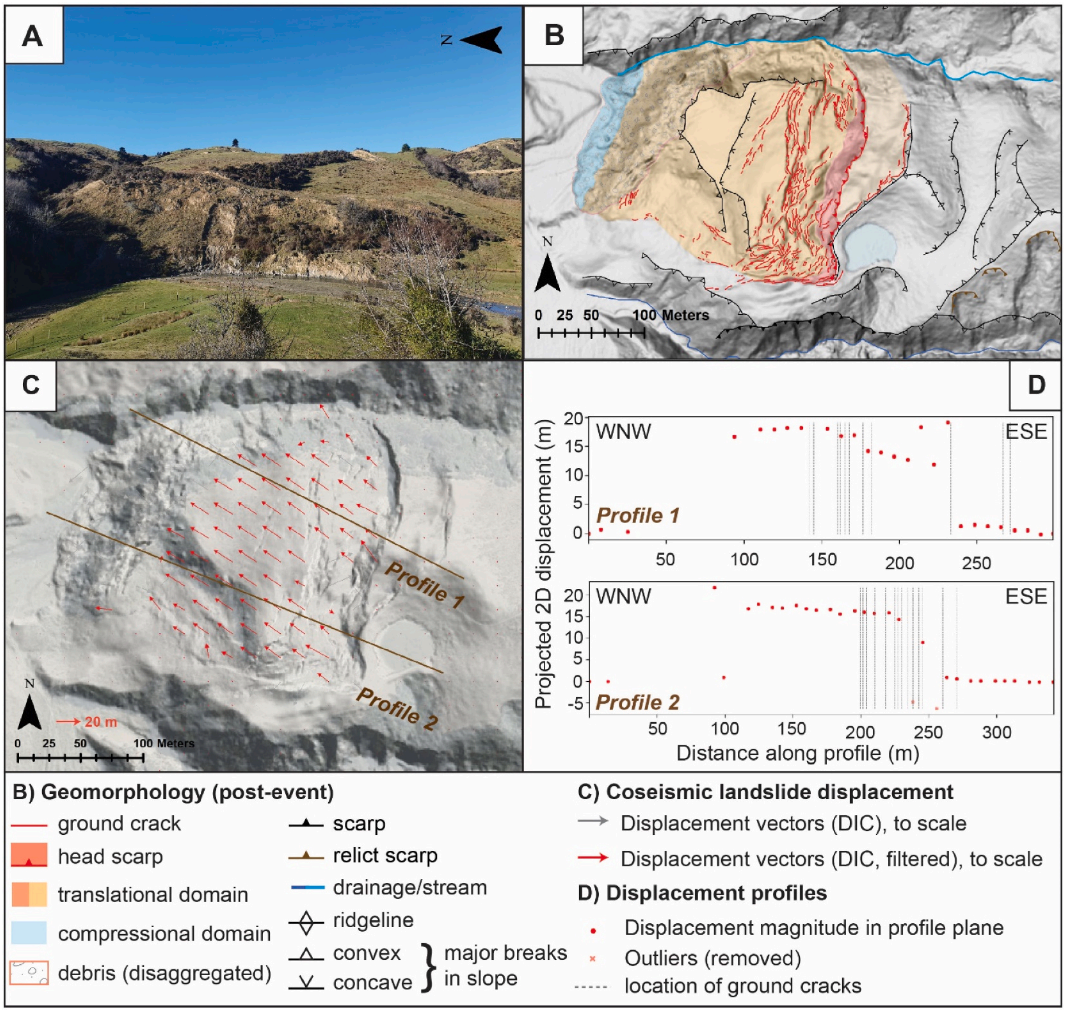

Fig. 10. Stanton River East landslide in North Canterbury (A) and mapped geomorphology (B) based on the post-earthquake 2016 DEM. Coseismic horizontal displacement vectors were projected on to two longitudinal profiles (C) and plotted in (D).

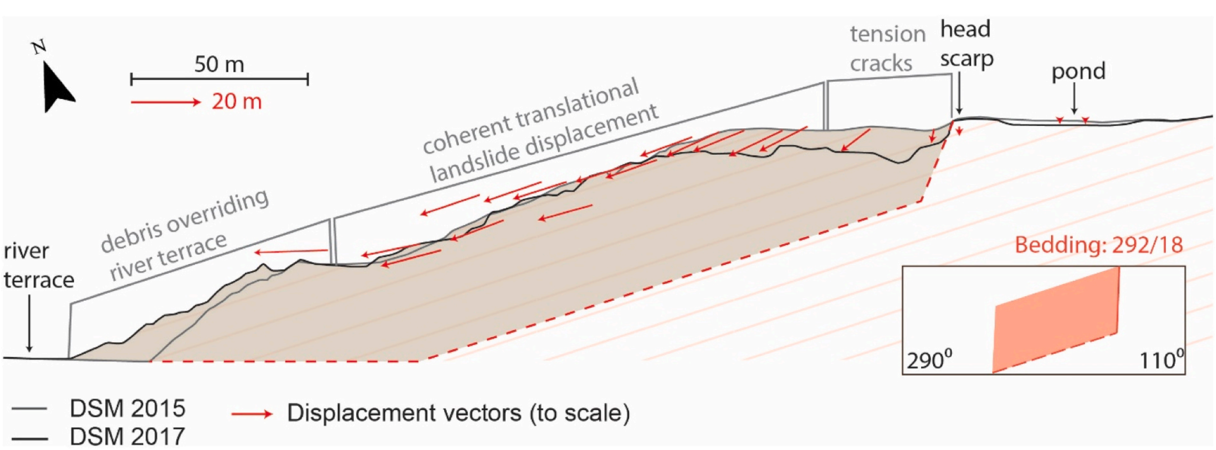

Fig. 11. Conceptual model of the planar translational rockslide at Stanton River East. Orientations of bedding were taken in the field and joint sets are given as (dip direction/dip).

in the 2015 orthoimage and DSM, we further interpret that this landslide initiated prior to the 2016 Kaikōura earthquake and was reactivated during the event.

5. Discussion

5.1. Synthesis of observed failure mechanisms

Based on the conceptual models presented above (Figs. 6, 9, and 11), we identified two failure mechanisms (Fig. 12). The failure mechanism of the incipient Okiwi Bay landslide and the Mt. Peter South landslide, both located in greywacke rock mass, were interpreted to be at different stages of a joint-step-path failure mechanism (Fig. 12A). The planar sliding mechanism of the Stanton River East landslide along persistent bedding planes in Neogene siltstone, on the other hand, is markedly different (Fig. 12B). Consistent with initial interpretations of how slopes failed during the Kaikōura earthquake (Massey et al., 2018b), the joint-step path failure mechanism (representative of failures in closely jointed greywacke rock mass without large-scale persistent discontinuities, Fig. 12A) and planar translational rockslides (representative of structurally controlled failures in Neogene sedimentary rocks, Fig. 12B) could combined represent the failure mechanism for c. 80 % of failures from the Kaikōura earthquake.

5.1.1. Joint-step-path failure mechanism

The first failure mechanism, Failure Mechanism A (Fig. 12), observed in greywacke rock mass without persistent discontinuities, can be divided into three failure stages: incipient sliding, transitional sliding, and avalanching. In an incipient landslide of this type - as seen at Okiwi Bay (Fig. 7D) and the southern portion of the Mt. Peter South site (Fig. 4D, Profile 2) - the displacement pattern along profile resembles a bell-curve (Fig. 12 A1). The displacement gradually increases below the head scarp, reaches a maximum in the central slope and subsequently

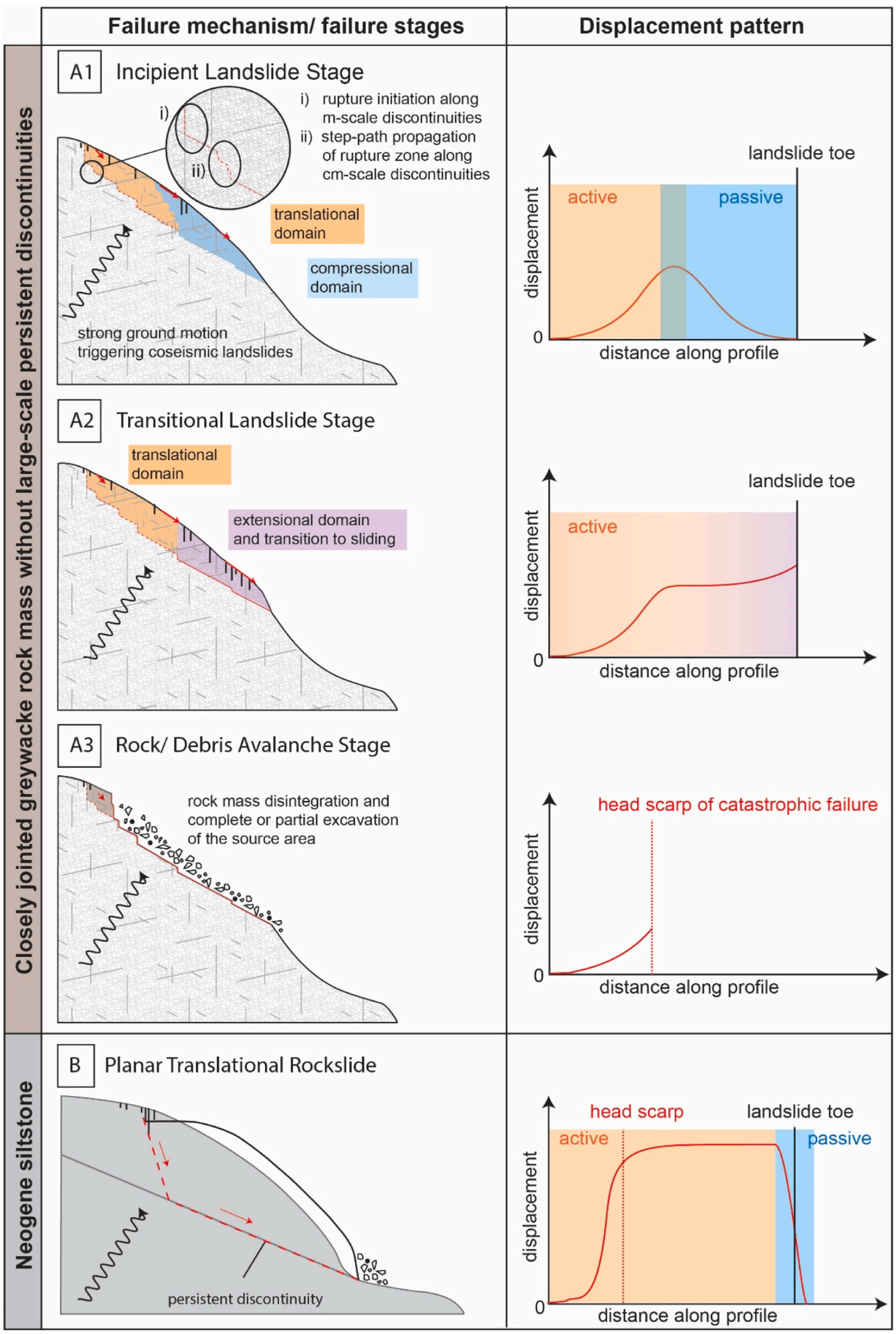

Fig. 12. (Left) Evolution of joint-step-path failures in closely jointed greywacke rock mass without persistent discontinuities in three failure stages (A1–3) and failure mechanism of Neogene siltstone as a planar translational rockslide (B). (Right) Conceptualised displacement patterns associated with individual failure stages/mechanism.

decreases gradually towards the toe of the landslide. This displacement pattern leads to internal deformation of the landslide mass. Tension cracks and scarps are present in the upper part of the slope at Okiwi Bay and Mt. Peter South and compressional deformation such as counter-scarps and bulging were observed in the lower part of the slope at Mt. Peter South. This suggests that the deformation of the incipient landslide is *actively* driven from the top of the slope while the lower portion of the slope *passively* resists the deformation (Fig. 12A). Compressive strain accumulates in the passive zone as long as the rupture plane has not fully developed (Kvapil and Clews, 1979). Based on the analysis of structural discontinuity mapping and subsurface information from geophysical surveys at the sites Okiwi Bay and Mt. Peter South, we interpret that the rupture plane likely initiates along m-scale discontinuities and propagates downslope, stepping through cm-scale defects between the m-scale persistent discontinuities. Based on GSI range (c. 40–55), failure in this type of rock mass is typically controlled by a network of non-persistent fractures (Brideau et al., 2009), which allows rupture propagation through multiple degrees of kinematic freedom. This agrees with our interpretation of a joint-step-path failure mechanism. The volume of these failures is likely limited by the increasing interlocking of the heavily jointed rock mass with depth. Propagation of the failure surface thus occurs along a depth-limited preferential joint-step-path and daylighting of the failure surface is controlled by topography. As a result, joint step path failures are relatively shallow and preferentially occur in the upper part of hillslopes.

In the transitional stage, which commences when the failure surface is fully developed and daylights at the landslide toe, sliding transitioning to avalanching can occur in the lower part of the slope as observed in the northern portion of the Mt. Peter South landslide (Fig. 12 A2). This means that the compressional deformation domain identified in the incipient landslide stage transitions to extensional deformation and, ultimately, translational sliding occurs. At this stage, the characteristic displacement pattern along profile becomes stepped. Like in the incipient landslide stage, the first increase in displacement magnitude is located downslope of the head scarp. The displacement magnitudes remain relatively constant in the translational domain and increase exponentially into the extensional domain upslope of the debris avalanche head scarp. At Mt. Peter South, the extensional domain is characterised by intense tension cracking and ground deformation increases closer to the head scarp of the debris avalanche (Fig. 4D, Profile 1).

In the third and final stage (Fig. 12 A3), avalanching and complete or partial excavation of the landslide material from the source area may occur. In this failure stage, the displacement profile is no longer measurable using the techniques applied here, but tension cracks and low magnitude displacement may be observed above the head scarp of the vacated source area. This failure stage is representative of many greywacke landslides that occurred in the steep slopes of the Seaward Kaikōura Ranges during the 2016 Kaikōura earthquake (Massey et al., 2020b). The described failure stages refer to the evolution of joint-step-path failures, which, as observed at the Mt. Peter South site, might occur contemporaneously in different portions of the landslide based on variability of topographic conditions and rock mass properties.

Globally, it has been found that earthquake-induced landslides in steep topography tend to cluster at ridge crests (Meunier et al., 2008; Fan et al., 2019). The topographic prerequisite for joint-step path failure - which can only occur in the described three failure stages if the landslide toe is located above the valley floor - is thus satisfied if topography is steep and local slope relief high. Joint-step-path failure could, therefore, be relevant in any active tectonic setting with steep topography where a closely jointed rock mass without large scale persistent discontinuities may be affected by strong earthquake shaking.

5.1.2. *Planar translational rockslide*

The second failure mechanism, Failure Mechanism B (Fig. 12) was observed at the Stanton River East landslide in massive, but weak Neogene siltstone and can be classified as a structurally controlled planar translational rockslide. This failure mechanism is characterised by coherent displacement of the landslide that follows the dip of one or more persistent discontinuities (in this case bedding) acting as the basal sliding zone. We observed this pattern of displacement in the Stanton River East landslide where a favourably oriented bedding plane readily explains the occurrence of the landslide and its failure mechanism (Figs. 10 and 11). Tension cracks are expected to occur close to the head scarp where the landslide mass detaches from the in-situ bedrock through failure of intact rock. The toe of the landslide is likely marked by bulging where the landslide mass overrides pre-existing topography (i.e. indicating compressional deformation) as we observed at the Stanton River East landslide (Fig. 10).

5.2. *Failure mechanism and landslide initiation processes*

Initiation of permanent displacement, by definition, occurs when stress exceeds strength (Jaeger et al., 2007). However, the physical processes causing initiation and failure propagation may differ depending on rock mass properties, slope geometry and triggering events. Here, we qualitatively discuss possible links between failure mechanisms and physical initiation processes based on the detailed characterisation of the two failure mechanisms described above.

In a joint-step-path failure (Fig. 12A), a network of m-scale and cm-scale discontinuities controls the failure. Initiation of the failure occurs in the upper portion of the slope primarily on favourably oriented m-scale discontinuities and the failure plane likely propagates along cm-scale joints in between the more persistent discontinuities. Initiation of movement in the upper slope suggests that slope stability may be particularly sensitive to physical processes that disproportionately influence the upper slope, mainly topographic amplification of strong ground motions (e.g. Meunier et al., 2008; Rault et al., 2019). During an earthquake, slope crests can experience high transient seismic stresses due to topographic amplification effects (Murphy, 2006). This ground motion amplification is further related to material impedance contrasts in the highly fractured, weathered, and heterogeneous greywacke rock mass (Eberhardt et al., 2004; Gischig et al., 2015). Topographic amplification of 1.4× free-field PGA can be expected for slopes steeper than 30° and 30 m high with the amplification factor expected to increase to 1.6× if impedance contrasts are present (CEN, 2004).

In contrast, a planar translational rockslide is reliant on persistent discontinuities acting as zones along which sliding occurs and landslide initiation is largely controlled by the properties of the materials within which sliding occurs. Due to concentration of topographic stresses at the base of the slope, landslides of this type are likely to initiate at the base of the slope. This can cause the occurrence of a deep-seated basal sliding plane. Planar translational rockslides therefore tend to be large and involve entire hillslopes. Initiation could occur through seismic forcing or static changes affecting the stress state within the slide-surface zone (s) from e.g., loading/unloading of the slope, pore pressure changes, fluvial incision/erosion. Previous work on large landslides in Neogene siltstone in New Zealand has shown that changes in rainfall-induced pore-water pressure critically influence landslide displacement (Massey et al., 2013; Massey et al., 2016). Furthermore, many of the landslides in Neogene siltstone that moved during the 2016 Kaikōura earthquake were re-activated pre-existing failures (Massey et al., 2018b). While a combination of rainfall events, pore pressure changes, fluvial incision, and strong ground motion clearly play an important role in the evolution of these landslides, further research is necessary to draw more significant conclusions about the factors that trigger initial movement.

The two distinct failure mechanisms were demonstrably controlled by two fundamentally different lithologies. Cretaceous greywacke rock slopes are heavily fractured due to intense tectonic deformation whereas the younger Neogene siltstones are less deformed and bedding is typically consistent on $>10^0$–10^2 m scales (Rattenbury et al., 2006). These differences in degrees of rock mass damage between the two lithologies result in the characteristic structure of the rock mass that controls rock slope failure mechanism, and, in turn, is intrinsically linked to initiation processes. The lithologic and structural control on failure mechanisms thus also has implications on volumes and hillslope positions of coseismic landslides, as has been found previously by Rault et al. (2019).

5.3. Implications for coseismic landslide susceptibility modelling

Our results have several key implications for coseismic landslide susceptibility models. First, the displacement analysis presented here demonstrates some challenges facing physics-based landslide susceptibility models based on Newmark sliding block analysis or other similar analyses. In these models, Newmark displacements are calculated based on material strength, topography and ground motion characteristics and the prediction of landslide occurrence is based on a displacement threshold. Jibson (2011) points out that the critical displacement threshold needs to be selected for each study according to material characteristics and the relevant definition of failure. In the literature, displacement thresholds for landslide occurrence are typically set regarding the critical displacement leading to macroscopic ground cracking and range between 5 cm and 15 cm (Wieczorek et al., 1985; Jibson, 1993; Abramson, 2002; Jibson, 2011; Dreyfus et al., 2013; Grant et al., 2016). This threshold is relevant for structures built on slopes that might be affected by deformation in landslide source areas. In the broader context of regional hazard and risk assessment, however, a larger threshold indicating the transition between incipient landslides and avalanches might arguably become more relevant. In this study, we found average 3D displacements at the incipient portion of the Mt. Peter South landslide and the incipient Okiwi Bay landslide of 6.4 m and 3.0 m, respectively. At Mt. Peter South, avalanching failure and rock mass disintegration occurred at displacement magnitudes of >11.6 m. In contrast, the Stanton River East landslide experienced coherent block movement with an average displacement of 16.8 m. These results highlight that the amount of displacement that can be accommodated before a transition from intact sliding to disaggregated avalanching occurs depends on the characteristics of the landslide material and topographic constraints. In highly jointed greywacke, relatively little displacement leads the rock mass to disintegrate whereas, in the weak but massive siltstone, fracture propagation through intact rock and rock mass deformation is needed before avalanching can occur.

Moreover, the amount of rock mass deformation associated with displacement magnitudes may vary between different sites and displacement magnitudes may not be the best metric to use as a threshold indicating a transition between failure stages. Instead, a strain-dependent threshold may be more appropriate. Based on failure mechanism, displacement can be accommodated through different modes of deformation. In greywacke rock mass, joint-step-path failure causes displacement to be accommodated along a basal rupture zone in the translational domain, whereas displacement in the compressional and extensional domain is accommodated through distributed rock mass deformation (Fig. 12A). In these failures, a measure of compressional strain, indicative of passive deformation needed for the rock mass to disintegrate, could therefore be a useful threshold metric. In contrast, translation of a coherent landslide body is dominant in Neogene siltstone, resulting in localisation of shear strain along a basal sliding zone controlled by bedding planes (i.e. shear strain is a function of landslide displacement and basal sliding zone thickness) (Fig. 12B). The evolution of these translational rock slides into avalanches is, therefore, expected to be mainly controlled by topographic constraints and the same threshold metric may not be meaningful. Consequently, the definition of a threshold indicating the transition between incipient landslides and avalanches needs to consider strain accumulation specific to individual failure mechanism. Such a threshold could serve as a valuable tool in the context of physics-based regional landslide hazard analysis.

Our results also highlight that site-specific studies remain an important tool to inform regional-scale coseismic landslide susceptibility models. Based on the conceptual models of landslides triggered by the 2016 Kaikōura earthquake, we infer that the orientations of m-scale discontinuities, slope angle, rock mass strength, and, potentially, amplification effects due to seismic shaking are relevant factors controlling slope stability in the greywacke rock mass without persistent discontinuities (Failure mechanism A, Fig. 12). On the other hand, bedding orientations relative to slope, strength of bedding planes, pore pressure along the basal sliding plane, and fluvial incision causing the daylighting (or near-daylighting) of bedding planes are key factors determining landslide susceptibility in planar rockslides in Neogene siltstone (Failure mechanism B, Fig. 12). This interpretation agrees with Williams et al. (2021), who found that slope-bedding alignment and fluvial incision are key susceptibility factors for landslide occurrence in weak sandstone and mudstone units where bedding provides preferential failure surfaces.

Domains of different failure mechanisms should therefore be considered when selecting landslide susceptibility factors. Geology is often used as a variable in statistics-based models (Reichenbach et al., 2018) and because failure mechanisms are largely controlled by rock mass characteristics, the parameter provides a good first-order distinction of failure mechanism domains. Statistics-based susceptibility models could be improved, however, by tailoring all susceptibility variables to specific failure domains. For this to be possible, systematic documentation of failure mechanism is required in earthquake-induced landslide inventories and we recommend that failure mechanism be routinely recorded as an attribute in future studies.

In the absence of field data, remote mapping as well as analysis of displacement patterns, as presented here, may aid in defining failure mechanisms. Profiles of the failures in highly jointed Torlesse greywacke show bell-shaped displacement in the incipient landslide stage, followed by stepped profiles in the transitional stage that eventually become unresolvable when the failure transitions into an avalanche (Fig. 12A). On the other hand, the Neogene siltstone rockslide shows a consistent and homogeneous displacement pattern of the majority of the landslide body (Fig. 12B).

6. Conclusions

Based on detailed site characterisation including displacement analysis, field and remote mapping, and geophysical surveys, we developed conceptual models for three landslides triggered by the 2016 Kaikōura earthquake. Analysis of two incipient landslides in Torlesse greywacke illustrate the failure stages of a rock mass comprising multiple sets of closely-spaced and low-persistent discontinuities while a landslide in Neogene siltstone exemplifies the role of high persistence bedding planes generating large planar translational rockslides. Based on our observations, we propose that the rupture plane of the two greywacke failures initiated close to the ridgetop where dynamic stresses from topographic amplification are generally strongest. In contrast, the landslide in Neogene siltstone initiated by sliding along a weak, high persistence, bedding plane. In this case, bedding-slope alignment plays an important role in landslide susceptibility.

Our results demonstrate that landslide susceptibility and failure mechanism vary significantly based on geology type and highlight the need to distinguish failure mechanism domains for regional landslide susceptibility models. The characteristic spatial displacement patterns we observe in the different failure mechanisms may be helpful for remotely identifying the relevant failure mechanisms for these regional models. Finally, as demonstrated by our analysis, the amount of displacement that can be accommodated before a failure transitions from sliding to avalanching, is highly dependent on material characteristics and topographic constraints.

Declaration of competing interest

The authors declare that they have no known competing financial or personal interests that could have influenced the work reported in this paper.

Data availability

Data will be made available on request.

Acknowledgements

This work was funded by the New Zealand government as part of the Ministry of Business, Innovation and Employment Endeavour project "Earthquake Induced Landscape Dynamics" and supported by the New Zealand Earthquake Commission. The authors would like to thank Thomas Brakenring, Giovanni Pradel (GNS Science), Adil Hameed, and Jivyde Despoj (University of Auckland) for their great help in the field. Additionally, we thank Monica Ghirotti and an anonymous reviewer for their constructive comments.

Appendix A. Supplementary data

Supplementary data to this article can be found online at https://doi.org/10.1016/j.geomorph.2022.108386.

References

Abramson, L.W., 2002. Slope Stability and Stabilization Methods, 2nd ed. Wiley, New York.

Agliardi, F., Crosta, G.B., Meloni, F., Valle, C., Rivolta, C., 2013. Structurally-controlled instability, damage and slope failure in a porphyry rock mass. Tectonophysics 605, 34–47. https://doi.org/10.1016/j.tecto.2013.05.033.

Archie, G.E., 1942. The Elecrical Resistivity Log as an Aid in determining some Reservoir Characteristics. Trans. Am. Inst. Min. Metall. Pet. Eng. 146, 54–62. https://doi.org/10.2118/942054-G.

Benites, R.A., Haines, A.J., 1994. Quantification of Seismic Wavefield Amplification by Topographic Features. Institute of Geological & Nuclear Sciences, Wellington NZ.

Bickel, V., Manconi, A., Amann, F., 2018. Quantitative assessment of digital image correlation methods to detect and monitor surface displacements of large slope instabilities. Remote Sens. 10 (6) https://doi.org/10.3390/rs10060865.

Bilderback, E.L., Pettinga, J.R., Litchfield, N.J., Quigley, M., Marden, M., Roering, J.J., Palmer, A.S., 2015. Hillslope response to climate-modulated river incision in the Waipaoa catchment, East Coast North Island, New Zealand. Geol. Soc. Am. Bull. 127 (1–2), 131–148. https://doi.org/10.1130/b31015.1.

Bloom, C.K., Howell, A., Stahl, T., Massey, C., Singeisen, C., 2021. The influence of off-fault deformation zones on the near-fault distribution of coseismic landslides. Geology 50 (3), 272–277. https://doi.org/10.1130/g49429.1.

Bradley, B.A., Razafindrakoto, H.N.T., Polak, V., 2017. Ground-Motion Observations from the 14 November 2016 Mw 7.8 Kaikoura, New Zealand, earthquake and Insights from Broadband Simulations. Seismol. Res. Lett. 88 (3), 740–756. https://doi.org/10.1785/0220160225.

Brain, M.J., Moya, S., Kincey, M.E., Tunstall, N., Petley, D.N., Sepúlveda, S.A., 2021. Controls on post-seismic landslide behavior in brittle rocks. J. Geophys. Res. Earth Surf. 126 (9) https://doi.org/10.1029/2021jf006242.

Brideau, M.-A., Yan, M., Stead, D., 2009. The role of tectonic damage and brittle rock fracture in the development of large rock slope failures. Geomorphology 103 (1), 30–49. https://doi.org/10.1016/j.geomorph.2008.04.010.

Brideau, M.-A., Massey, C.I., Carey, J.M., Lyndsell, B., 2020. Geomechanical characterisation of discontinuous greywacke from the Wellington region based on laboratory testing. N. Z. J. Geol. Geophys. 1–18 https://doi.org/10.1080/00288306.2020.1853181.

CEN, 2004. Eurocode 8: Design of Structures for Earthquake Resistance - Part 5: Foundations, Retaining Structures Ad Geotechnical Aspects EN 1998–5:2004. The European Union, Brussels.

Cody, E., Draebing, D., McColl, S., Cook, S., Brideau, M.-A., 2019. Geomorphology and geological controls of an active paraglacial rockslide in the New Zealand Southern Alps. Landslides 17 (4), 755–776. https://doi.org/10.1007/s10346-019-01316-2.

Dafni, J., Wartman, J., 2021. Centrifuge studies of topographic effects: parametric investigation. Bull. Seismol. Soc. Am. https://doi.org/10.1785/0120200354.

Dellow, S., Massey, C., Cox, S., Archibald, G., Begg, J., Bruce, Z., Carey, J., et al., 2017. Landslides caused by the Mw7.8 Kaikōura earthquake and the immediate response. Bull. New Zealand Soc. Earth. Eng. 50 (2), 106–116. https://doi.org/10.5459/bnzsee.50.2.106-116.

Donati, D., Westin, A.M., Stead, D., Clague, J.J., Stewart, T.W., Lawrence, M.S., Marsh, J., 2021. A reinterpretation of the Downie Slide (British Columbia, Canada) based on slope damage characterization and subsurface data interpretation. Landslides. https://doi.org/10.1007/s10346-020-01601-5.

Dreyfus, D., Rathje, E.M., Jibson, R.W., 2013. The influence of different simplified sliding-block models and input parameters on regional predictions of seismic landslides triggered by the Northridge earthquake. Eng. Geol. 163, 41–54. https://doi.org/10.1016/j.enggeo.2013.05.015.

Duffy, B., 2008. Development of Multichannel Analysis of Surface Waves (MASW) for Characterising the Internal Structure of Active Fault Zones as a Predictive Method of Identifying the Distribution of Ground Deformation. University of Canterbury. MSc Thesis.

Eberhardt, E., Stead, D., Coggan, J.S., 2004. Numerical analysis of initiation and progressive failure in natural rock slopes—the 1991 Randa rockslide. Int. J. Rock Mech. Min. Sci. 41 (1), 69–87. https://doi.org/10.1016/s1365-1609(03)00076-5.

Elmo, D., Donati, D., Stead, D., 2018. Challenges in the characterisation of intact rock bridges in rock slopes. Eng. Geol. 245, 81–96. https://doi.org/10.1016/j.enggeo.2018.06.014.

Fan, X., Scaringi, G., Korup, O., West, A.J., Westen, C.J., Tanyas, H., Huang, R., 2019. Earthquake-induced chains of geologic hazards: patterns, mechanisms, and impacts. Rev. Geophys. 57 (2), 421–503. https://doi.org/10.1029/2018rg000626.

Fisher, R.A., 1953. Dispersion on a sphere. Proc. R. Soc. Lond. 2017 (1130), 295–305. https://doi.org/10.1098/rspa.1953.0064.

Gallen, S.F., Clark, M.K., Godt, J.W., 2014. Coseismic landslides reveal near-surface rock strength in a high-relief, tectonically active setting. Geology 43 (1), 11–14. https://doi.org/10.1130/g36080.1.

Gerber, E., Scheidegger, A.E., 1969. Stress-induced weathering of rock masses. Eclogae Geol. Helv. 62, 401–415. https://doi.org/10.5169/seals-163705.

Gischig, V.S., Eberhardt, E., Moore, J.R., Hungr, O., 2015. On the seismic response of deep-seated rock slope instabilities — insights from numerical modeling. Eng. Geol. 193, 1–18. https://doi.org/10.1016/j.enggeo.2015.04.003.

Gischig, V., Preisig, G., Eberhardt, E., 2016. Numerical investigation of seismically induced rock mass fatigue as a mechanism contributing to the progressive failure of deep-seated landslides. Rock Mech. Rock. Eng. 49 (6), 2457–2478. https://doi.org/10.1007/s00603-015-0821-z.

Grämiger, L.M., Moore, J.R., Gischig, V.S., Ivy-Ochs, S., Loew, S., 2017. Beyond debuttressing: mechanics of paraglacial rock slope damage during repeat glacial cycles. J. Geophys. Res. Earth Surf. 122 (4), 1004–1036. https://doi.org/10.1002/2016jf003967.

Grant, A., Wartman, J., Abou-Jaoude, G., 2016. Multimodal method for coseismic landslide hazard assessment. Eng. Geol. 212, 146–160. https://doi.org/10.1016/j.enggeo.2016.08.005.

Heincke, B., Maurer, H., Green, A.G., Willenberg, H., Spillmann, T., Burlini, L., 2006. Characterizing an unstable mountain slope using shallow 2D and 3D seismic tomography. Geophysics 71 (6), B241–B256. https://doi.org/10.1190/1.2338823.

Heincke, B., Günther, T., Dalsegg, E., Rønning, J.S., Ganerød, G.V., Elvebakk, H., 2010. Combined three-dimensional electric and seismic tomography study on the Åknes rockslide in western Norway. J. Appl. Geophys. 70 (4), 292–306. https://doi.org/10.1016/j.jappgeo.2009.12.004.

Hoek, E., Bray, J.W., 1981. Rock Slope Engineering, Rev. 3rd ed. Institution of Mining and Metallurgy, London.

Hoek, E., Brown, E.T., 1997. Practical estimates of rock mass strength. Int. J. Rock Mech. Min. Sci. 34 (8), 1165–1186. https://doi.org/10.1016/S1365-1609(97)80069-X.

Hoek, E., Marinos, P., 2000. Predicting tunnel squeezing problems in weak heterogeneous rock masses. Tunn. Tunn. Int. 32 (11), 45–51.

Howell, A., Nissen, E., Stahl, T., Clark, K., Kearse, J., Van Dissen, R., Villamor, P., Langridge, R., Jones, K., 2020. Three-dimensional surface displacements during the 2016 Mw 7.8 Kaikōura Earthquake (New Zealand) from photogrammetry-derived point clouds. J. Geophys. Res. Solid Earth 125 (1). https://doi.org/10.1029/2019jb018739.

Hungr, O., Leroueil, S., Picarelli, L., 2013. The Varnes classification of landslide types, an update. Landslides 11 (2), 167–194. https://doi.org/10.1007/s10346-013-0436-y.

ISRM, 1978. In: Suggested Methods for the Quantitative Description of Discontinuities in Rock Masses. Pergamon Press Ltd, Great Britain, pp. 319–368.

Jaeger, J.C., Cook, N.G.W., Zimmerman, R.W., 2007. Fundamentals of Rock Mechanics, 4th edition. Blackwell Publishing.

Jibson, R.W., 1993. Predicting earthquake-induced landslide displacement using Newmark's sliding block analysis. Transp. Res. Rec. 1411, 9–17.

Jibson, R.W., 2011. Methods for assessing the stability of slopes during earthquakes—a retrospective. Eng. Geol. 122 (1–2), 43–50. https://doi.org/10.1016/j.enggeo.2010.09.017.

Kansas Geological Survey, 2018. SurfSeis 6. Lawrence, KS.

Keefer, D.K., 1984. Landslides caused by earthquakes. Geol. Soc. Am. Bull. 95, 406–421.

Korup, O., 2004. Geomorphic implications of fault zone weakening: slope instability along the Alpine Fault, South Westland to Fiordland. N. Z. J. Geol. Geophys. 47 (2), 257–267. https://doi.org/10.1080/00288306.2004.9515052.

Krautblatter, M., Moore, J.R., 2014. Rock slope instability and erosion: toward improved process understanding. Earth Surf. Process. Landf. 39 (9), 1273–1278. https://doi.org/10.1002/esp.3578.

Krautblatter, M., Funk, D., Günzel, F.K., 2013. Why permafrost rocks become unstable: a rock-ice-mechanical model in time and space. Earth Surf. Process. Landf. 38 (8), 876–887. https://doi.org/10.1002/esp.3374.

Kvapil, R., Clews, K.M., 1979. An examination of the Prandtl mechanism in large-dimension slope failures. Trans. Inst. Mining Metall. Sect. A 88, A1–A5.

Langridge, R.M., Ries, W.F., Litchfield, N.J., Villamor, P., Van Dissen, R.J., Barrell, D.J.A., Stirling, M.W., 2016. The New Zealand active faults database. N. Z. J. Geol. Geophys. 59, 86–96. https://doi.org/10.1080/00288306.2015.1112818.

Litchfield, N.J., Villamor, P., Dissen, R.J.V., Nicol, A., Barnes, P.M., Barrell, A., J, D., Zinke, R., 2018. Surface rupture of multiple crustal faults in the 2016 Mw 7.8 Kaikōura, New Zealand, earthquake. Bulletin of the Seismological Society of America 108 (3B), 1496–1520. https://doi.org/10.1785/0120170300.

Loke, M.H., Dahlin, T., 2002. A comparison of the Gauss-Newton and quasi-Newton methods in resistivity imaging inversion. J. Appl. Geophys. 49 (3), 149–162. https://doi.org/10.1016/s0926-9851(01)00106-9.

Marc, O., Hovius, N., Meunier, P., Uchida, T., Hayashi, S., 2015. Transient changes of landslide rates after earthquakes. Geology 43 (10), 883–886. https://doi.org/10.1130/g36961.1.

Massey, C.I., Petley, D.N., McSaveney, M.J., 2013. Patterns of movement in reactivated landslides. Eng. Geol. 159, 1–19. https://doi.org/10.1016/j.enggeo.2013.03.011.

Massey, C.I., Petley, D.N., McSaveney, M.J., Archibald, G., 2016. Basal sliding and plastic deformation of a slow, reactivated landslide in New Zealand. Eng. Geol. 208, 11–28. https://doi.org/10.1016/j.enggeo.2016.04.016.

Massey, C., Della Pasqua, F., Holden, C., Kaiser, A., Richards, L., Wartman, J., Janku, L., 2017. Rock slope response to strong earthquake shaking. Landslides 14 (1), 249–268. https://doi.org/10.1007/s10346-016-0684-8.

Massey, C., Townsend, D., Dellow, G.D., Lukovic, B., Rosser, B., Archibald, G., Carey, J., 2018. Kaikoura earthquake Short-Term Project: landslide inventory and landslide dam assessments. GNS Sci. Report. https://doi.org/10.21420/G2FP82, 2018/19.

Massey, C., Townsend, D., Rathje, E., Allstadt, K.E., Lukovic, B., Kaneko, Y., Villeneuve, M., 2018b. Landslides Triggered by the 14 November 2016 Mw 7.8 Kaikōura Earthquake, New Zealand. Bull. Seismol. Soc. Am. 108 (3B), 1630–1648. https://doi.org/10.1785/0120170305.

Massey, C., Townsend, D., Lukovic, B., Morgenstern, R., Jones, K., Rosser, B., de Vilder, S., 2020. Landslides triggered by the MW 7.8 14 November 2016 Kaikōura earthquake: an update. Landslides. https://doi.org/10.1007/s10346-020-01439-x.

Massey, C.I., Townsend, D., Jones, K., Lukovic, B., Rhoades, D., Morgenstern, R., Olsen, M., 2020b. Volume characteristics of landslides triggered by the Mw 7.8 2016 Kaikōura Earthquake, New Zealand, derived from digital surface difference modelling. J. Geophys. Res. Earth Surf. 125 https://doi.org/10.1029/2019jf005163.

McColl, S.T., 2015. Landslide causes and triggers. In: Schroder, J.F., Davies, T. (Eds.), Landslide Hazards, Risks and Disasters, pp. 17–42.

Meunier, P., Hovius, N., Haines, J.A., 2008. Topographic site effects and the location of earthquake induced landslides. Earth Planet. Sci. Lett. 275 (3–4), 221–232. https://doi.org/10.1016/j.epsl.2008.07.020.

Murphy, W., 2006. The role of topographic amplification on the initiation of rock slopes failures during earthquakes. In: Evans, S.G. (Ed.), Landslides from Massive Rock Slope Failure, pp. 139–154.

Park, C.B., Miller, R.D., Xia, J., 1999. Multichannel analysis of surface waves. Geophysics 64 (3), 800–808.

Parker, R.N., Hancox, G.T., Petley, D.N., Massey, C.I., Densmore, A.L., Rosser, N.J., 2015. Spatial distributions of earthquake-induced landslides and hillslope preconditioning in the northwest south IslandNew Zealand. Earth Surface Dynamics 3 (4), 501–525. https://doi.org/10.5194/esurf-3-501-2015.

Pazzi, V., Morelli, S., Fanti, R., 2019. A review of the advantages and limitations of geophysical investigations in landslide studies. International Journal of Geophysics 2019. https://doi.org/10.1155/2019/298308.

Perrone, A., Lapenna, V., Piscitelli, S., 2014. Electrical resistivity tomography technique for landslide investigation: a review. Earth Sci. Rev. 135, 65–82. https://doi.org/10.1016/j.earscirev.2014.04.002.

Pollock, W., Grant, A., Wartman, J., Abou-Jaoude, G., 2019. Multimodal method for landslide risk analysis. MethodsX 6, 827–836. https://doi.org/10.1016/j.mex.2019.04.012.

Rattenbury, M.S., Townsend, D.B., Johnston, M.R., 2006. Geology of the Kaikoura Area. 1:250 000 Geological Map 13. GNS Science, Lower Hutt, New Zealand.

Rault, C., Robert, A., Marc, O., Hovius, N., Meunier, P., 2019. Seismic and geologic controls on spatial clustering of landslides in three large earthquakes. Earth Surf. Dyn. 7 (3), 829–839. https://doi.org/10.5194/esurf-7-829-2019.

Reichenbach, P., Rossi, M., Malamud, B.D., Mihir, M., Guzzetti, F., 2018. A review of statistically-based landslide susceptibility models. Earth Sci. Rev. 180, 60–91. https://doi.org/10.1016/j.earscirev.2018.03.001.

Reid, M.E., Christian, S.B., Brien, D.L., Henderson, S.T., 2015. Scoops3D: software to analyze 3D slope stability throughout a digital landscape. U.S. Geol. Survey Tech. Meth. 14-A1, 1–218. https://doi.org/10.3133/tm14A1.

Sandmeier, K.J., 2012. REFLEXW Version 7.0. Karlsruhe.

Stead, D., Wolter, A., 2015. A critical review of rock slope failure mechanisms: the importance of structural geology. J. Struct. Geol. 74, 1–23. https://doi.org/10.1016/j.jsg.2015.02.002.

Tanyaş, H., van Westen, C.J., Allstadt, K.E., Anna Nowicki Jessee, M., Görüm, T., Jibson, R.W., Hovius, N., 2017. Presentation and analysis of a worldwide database of earthquake-induced landslide inventories. Journal of Geophysical Research: Earth Surface 122 (10), 1991–2015. https://doi.org/10.1002/2017jf004236.

Terzaghi, K., 1962. Stability of steep slopes on hard unweathered rock. Géotechnique 12 (4), 251–270. https://doi.org/10.1680/geot.1962.12.4.251.

Upton, P., Koons, P.O., Roy, S.G., 2018. Rock failure and erosion of a fault damage zone as a function of rock properties: Alpine Fault at Waikukupa River. N. Z. J. Geol. Geophys. 61 (3), 367–375. https://doi.org/10.1080/00288306.2018.1430592.

Van Houtte, C., Bannister, S., Holden, C., Bourguignon, S., McVerry, G., 2017. The New Zealand strong motion database. Bull. N. Z. Soc. Earthq. Eng. 50 (1), 1–20. https://doi.org/10.5459/bnzsee.50.1.1-20.

Viles, H.A., 2013. Linking weathering and rock slope instability: non-linear perspectives. Earth Surf. Process. Landf. 38 (1), 62–70. https://doi.org/10.1002/esp.3294.

Whiteley, J.S., Chambers, J.E., Uhlemann, S., Wilkinson, P.B., Kendall, J.M., 2019. Geophysical monitoring of moisture-induced landslides: a review. Rev. Geophys. 57, 106–145. https://doi.org/10.1029/2018RG000603.

Wieczorek, G.F., Wilson, R.C., Harp, E.L., 1985. Map Showing Slope Stability During Earthquakes in San Mateo County. USGS, California. https://doi.org/10.3133/i1257E.

Williams, F., McColl, S., Fuller, I., Massey, C., Smith, H., Neverman, A., 2021. Intersection of fluvial incision and weak geologic structures cause divergence from a universal threshold slope model of landslide occurrence. Geomorphology 389 (15). https://doi.org/10.1016/j.geomorph.2021.107795.

Zinke, R., Hollingsworth, J., Dolan, J.F., Van Dissen, R., 2019. Three-dimensional surface deformation in the 2016 MW 7.8 Kaikōura, New Zealand, earthquake from optical image correlation: implications for strain localization and long-term evolution of the Pacific-Australian plate boundary. Geochem. Geophys. Geosyst. 20 (3), 1609–1628. https://doi.org/10.1029/2018gc007951.